5-2017

Processing-property-structure relationships of carbonaceous materials derived from renewable lignin products

Valerie García-Negrón
University of Tennessee, Knoxville, vgarcian@utk.edu

To the Graduate Council:

I am submitting herewith a thesis written by Valerie García-Negrón entitled "Processing-property-structure relationships of carbonaceous materials derived from renewable lignin products." I have examined the final electronic copy of this thesis for form and content and recommend that it be accepted in partial fulfillment of the requirements for the degree of Master of Science, with a major in Materials Science and Engineering.

David J. Keffer, Major Professor

We have read this thesis and recommend its acceptance:

David P. Harper, Orlando Rios

Accepted for the Council:
Dixie L. Thompson

Vice Provost and Dean of the Graduate School

(Original signatures are on file with official student records.)

Processing-property-structure relationships of carbonaceous materials derived from renewable lignin products

A Thesis Presented for the
Master of Science
Degree
The University of Tennessee, Knoxville

Valerie García-Negrón

May 2017

DEDICATION

This work is dedicated to my family who has been always present throughout each step of my life. To my parents, Alberto and Idalia, I am thankful for the exemplary discipline and love you both have provided since I was young. To my brothers, Greg and Jomar, I give thanks for your continuous support and love you provide.

Lastly, I want to extend my sincerest gratitude to my best friend, Eduardo M. Ponce Mojica. Thanks for your unconditional support and kindness. I wish you all the best in your career path and may God help us all to continue in our life journey.

ACKNOWLEDGMENTS

To my committee, thanks for the support and believing in this research. I am very fortunate to be working with this team. Thanks for giving me the opportunity to study and for allowing me to grow in a professional environment under professional supervision. Dr. David Harper, life can get difficult but you are always smiling at it and being positive at it; thanks for being an exemplary mentor and friend. I have learned so many things in such a short time. Words are not enough to express my sincerest gratitude for all your support, discipline, and patience. Dr. Orlando Rios, thanks for helping during the process of completing graduate school. I could have not done any of this without your guidance, discipline, and support. I am grateful for your help and your professional research experience. Dr. David Keffer, you are one of a handful of people who has impacted my life with discipline and hard work; thanks for helping and spending office hours to make this research writing possible. You did motivate me a lot when I had doubts. Lastly, I would like to thank Dr. Jianlin Li, Dr. David Wood, Dr. Claus Daniel, Dr. Gabriel Veith, Dr. Omid Hosseinaei, Dr. Nicole Labbé, Dr. Nourredine Abdoulmoumine, Mr. Chris Helton and Mr. Nathan Phillip for research support. I also as well want to thank all my friends from the Center for Renewable Carbon (CRC) and the Materials Science and Engineering department.

ABSTRACT

Efforts to effectively use lignin, a by-product of paper and biofuels production, have been carried out for several decades. This renewable resource has potential for use as a carbonaceous material due to its aromatic structure and high carbon content, reminiscent of graphite. The search for new carbon-based materials is extremely active, because they are necessary components in many applications, such as energy storage, electronics, catalysis, and lubricants. Traditional carbon-based materials are derived or mined from petroleum or coal, thus, contributing to pollution, national security risks, and anthropogenic climate change. Lignin, a carbon-rich component found in the tissues of vascular plants, is commercially available as a waste product from pulp and biofuels industries. The main processing stages involved in converting raw lignin into a viable product are lignin extraction, carbonization treatments, physiochemical characterization, and application testing. Lignin is a complex amorphous macromolecule difficult to predict and these studies attempt to identify its processing-structure-property relationships. Due to the tremendous growth in demand for graphite, the United States is stimulating research efforts to produce and synthesize an alternate material.

The first part of this study involved processing kraft softwood lignin to make lignin-based anodes for low-cost, high-efficiency lithium-carbon batteries. The processing variables under investigation included the presence, temperature, and duration of thermal stabilization, pyrolysis, and reduction. Materials were characterized at the atomic- and micro-scales. Under optimal processing conditions, a coin cell with a lignin-based anode demonstrated capacity superior to the theoretical maximum capacity of 372 mAh/g [miliampere hour per grams] for graphite.

The second part of this study consisted on understanding structural relationships between green lignin feedstock and the resulting carbon composites, via a suite of characterization techniques. Small angle neutron scattering experiments were performed to understand and visualize structural orientation of green lignin fibers. Raman spectroscopy provided insight of the high degree of ordering and disorder of graphitic structure from carbonized fibers. Moreover, different types of lignin helped predict structural relationships between lignin sources, extraction methods, such as kraft

and organosolv, and processing. These relationships dictate the resulting carbon structure, its mechanical properties, and its suitability for specific applications.

PREFACE

This manuscript is composed of four chapters: an overall introduction, two research articles, and an overall conclusion. The first research article is an extended version of a manuscript published in “Energy Technology” and the second article is related to an in-progress publication. Although each article can be used as a stand-alone unit, incorporating them as chapters provides a framework to present clearly the main research objectives of this study.

Chapter 1 provides an overview of lignin sources, lignin structural characteristics, and lignin extraction methods. These topics are enriched with background material and literature references to allow the reader to understand the importance of lignin structure and the innovative aspects of this study.

Chapter 2 focuses on the processing techniques used for the carbonization of kraft softwood lignin (KSL). Sample preparations and material graphitic characterization are presented in detail to help pair processing-structure-property relationships. Lignin carbon anodes were built as an electrochemical application of such materials. The processing techniques and material characterization were performed at the Center for Renewable Carbon at University of Tennessee-Knoxville (UTK) and Oak Ridge National Laboratory (ORNL). Electrochemical experiments were performed at the National Transportation Research Center at Oak Ridge National Laboratory (NTRC-ORNL) facilities with the collaboration of Dr. Jianlin Li, Dr. Claus Daniel, Dr. David Wood, Dr. Orlando Rios, and Mr. Nathan Phillip.

Chapter 3 presents a study of small angle neutron scattering and Raman spectroscopy using various sample compositions as means to relate lignin linkages with fiber structure, pore distributions, and degree of graphitization. These experiments were the result of collaboration with Dr. Sai Venkatesh Pingali (ORNL) and a UTK group, including Dr. Stephen Chmely, Dr. David Harper, and Dr. Timothy Rials.

Chapter 4 presents concluding remarks, relating outcomes of the various lignin experiments conducted. Also, future research objectives that will allow a more in-depth understanding of lignin carbonaceous materials are outlined.

TABLE OF CONTENTS

LIST OF TABLES

LIST OF FIGURES

ABBREVIATIONS AND SYMBOLS

Ar = Argon
BET = Brunauer-Emmett-Teller
C = Carbon
CO_2 = Carbon dioxide
CRC = Center for Renewable Carbon
D_2O = Deuterium oxide
H = Hydrogen
HD pentane = H (hydrogenated pentane) and D (deuterated pentane)
HS = High severity
HW = Hardwood
K = Potassium
KSL = Kraft softwood lignin
Li = Lithium
LS = Low severity
Mg = Magnesium
N = Nitrogen
Na = Sodium
NaOH = Sodium hydroxide
NaS_2 = Sodium disulfide
NTRC = National Transportation Research Center
OCH_3 = Methoxyl
ORNL = Oak Ridge National Laboratory
pH = Potential of hydrogen
R_g = Radius of gyration
S = Sulfur
SAS = Small angle scattering
SANS = Small angle neutron scattering
SEM = Scanning electron microscopy
SG = Switchgrass lignin
Si = Silicon
Tg = Glass transition temperature
TGA = Thermogravimetric analyzer
UTK = University of Tennessee, Knoxville
USANS = Ultra small angle scattering
YP = Yellow poplar lignin
XRD = X-ray diffraction

CHAPTER 1
INTRODUCTION

LIGNIN IN NATURE

The main natural polymeric components found in the cell walls of trees and grasses are cellulose, hemicellulose, and lignin. These molecular compounds are responsible for important physicochemical characteristics, such as the structural integrity of the plants, moisture and nutrient movement, and protecting tissues from microorganisms. Lignin is the second most abundant natural polymer next to cellulose [1]. Lignin contains an abundance of phenyl propane groups leading to a relatively high carbon content (up to 60%) compared to other natural polymers [2]. The content of lignin depends on plant type, for example, softwoods (28%), hardwoods (20%), and grasses (19% stem, 14.5% leaf) [3]. For reference, cellulose content in softwoods and hardwoods is approximately 45%, and hemicellulose content is 17% in softwoods and 25% in hardwoods [1]. Switchgrass contains lignin (13.3–22.5%), cellulose (26.8–37.5%), hemicellulose (22.4–28.8%) [4, 5]. Some inorganic compounds found in biomass are: Ca, K, Mg, and Si, as well as some extractives and small amounts of proteins that only act as metabolic intermediates, energy store, and defense mechanism [5]. Lignin belongs to a class of complex polymers with cross-linked polysaccharides containing aliphatic, aryl, methoxyl, and phenol functional groups. Specifically, the functional groups with the greatest presence in lignin are carbonyl, carboxyl, ester, anhydride, aromatic carbon-oxygen (C-O), carbon-carbon (C-C), protonated aromatic C-C, aliphatic carbon-hydrogen (C-H), methoxyl (OCH_3), and aliphatic C-C [6]. In general, lignin is formed via polymerization of monomeric alcohols, principally, *p*-coumaryl, coniferyl, and sinapyl, refer to Figure 12 in Chapter 2.

The heterogeneous subunits (radical and polar) of lignin's polymers make it difficult to isolate in its natural form without any structural degradation. In the literature, some possible structures have been hypothesized [1]. Moreover, the structure of lignin may differ based on plant age, plant part, wood species, and processing conditions. Understanding the structural characteristics of lignin provides path to new products that are natural, renewable, and cost effective.

EXTRACTION METHODS FOR LIGNIN PRODUCTS

Kraft pulping process

Paper and cellulose-based materials are made from plant biomass with varying lignin concentrations. Pulp mills use pulping techniques for delignification and fiber isolation. Kraft processing is the most common chemical pulping method, due to its high yield of high tensile modulus fibers, and its ability to pulp softwoods [2]. Currently, commercial lignin is obtained as a by-product from the kraft process used in the papermaking industry. In kraft processing, as shown in Figure 1, the wood chips are cooked (digested) at high pressure, high temperature, and high pH level in a white liquor solution of sodium hydroxide (NaOH) and sodium disulfide (NaS_2). The digestive process can be performed in continuous or batch stages in a reactor. The pulp product is mainly desired for paper materials, where it is washed with water and milled. The black liquor is precipitated with acid and refined to produce kraft lignin, also called alkali or sulfate lignin. The remaining black liquor is removed and recycled to serve as fuel source for boiler operation during kraft processing [7].

Several variations of kraft processing stages have been studied. In one case study, kraft lignin was blended with poly(ethylene oxide) to compare hardwood and softwood lignin's miscibility and chemical properties. Based on Genco's studies, kraft hardwood lignin (KHL) revealed stronger hydrogen bonding but weaker intramolecular interaction between units. Kraft softwood lignin (KSL) has higher concentrations of aliphatic and biphenol hydroxyl groups but less aromatic hydroxyl and methoxyl groups when compared to KHL [2].

Organosolv fractionation

Cellulose can be separated from lignin by other pulping methods as well as the kraft process, such as soda, lignosulfonate, and organosolv [8]. Lignin macromolecules are altered by pre-treatments methods that aid pulping and may include steam explosion and ammonia fiber explosion (AFEX) [9]. Organosolv fractionation, which in comparison with kraft, produces relatively high purity lignin [10, 11]. Lignin purity of 90% can be achieved by organosolv fractionation, while a range from 29 to 45% is achieved by Kraft pulping [10, 12]. Lignin is insoluble in water and most alcohols and is only soluble in

some organic solvents or ionic liquids. However, organosolv's high cost, which is related to organic solvents and their recovery, makes it uncommon in the pulping industry [13]. The organosolv process makes use of neutral or acid catalysts at high pressure and high temperature (i.e. Alcell process) to break down lignocellulosic macromolecules into small fragments prior to the main dissolution step [10]. Aqueous ethanol, sulfides, and alkali alcohols are examples of delignification solvents [14]. These chemical processes are affected by both the solution pH and the solvent properties that enable lignin fragmentation and inhibit lignin re-condensation. Past studies have shown that lignin breakdown via hydrolysis and acid catalysis that mainly cleaves ether linkages, mainly β-ether bonds [15]. Both hydrolysable and highly reactive ether bonds are more prevalent in hardwoods than softwoods. Subsequent organosolv reactions form benzyl carbocation and phenolic hydroxyl groups such as guaiacol and β-hydroxyconiferyl alcohol [15]. Functional groups formed and release during wood processing differ on lignin type, pulping conditions, and lignin recovery method.

Clean fractionation is another organosolv pulping technology that uses a tertiary mixture of methyl isobutyl ketone (MIBK), ethanol (EtOH) and water, which result in higher selectivity and operational advantages when compared to other methods [10]. An advantage of clean fractionation is that it can isolate individual components and recover them with high purity and yield. Organosolv is also used for other applications such as fermentation of EtOH [16]. Moreover, the Alcell organosolv pre-treatment processes wood using aqueous ethanol solutions 40–60% (v/v) to high temperature of ~195 ˚C and recovers the solvent by flash evaporation [17]. The process produces pulp, acetic acid, liquor with low molecular lignin, hemicellulose, saccharides, and furfurals. After distillation, ethanol and furfurals are recovered, and Alcell lignin is obtained.

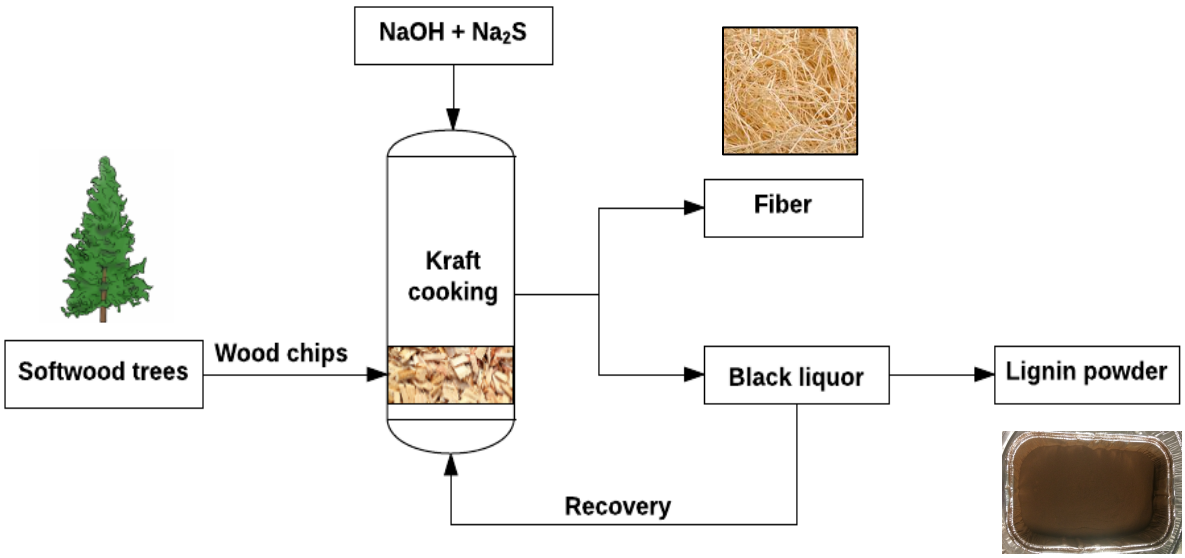

Figure 1. Kraft pulping process of softwood trees for lignin products. Softwood feedstocks are broken in a pulp mill into wood chips, and then cooked in a reactor using NaOH and NaS_2. This step results in a cellulose fiber that is mostly used for paper products, and black liquor that is commonly recycled for future kraft cooking. The black liquor can be evaporated, dried, and pulverized to extract lignin powder.

CHARACTERIZATION METHODS FOR LIGNIN

Lignin is an alkylaromatic complex polymer found mostly in wood that varies depending on biomass source. For example, softwoods contain guaiacyl (G) in abundance and some p-hydroxyphenyl (H). Hardwoods contain more syringyl (S) and some G, whereas grasses contain more H and mixture of G and S units. Lignin is found between and within cell walls providing a matrix for cellulose fibers. Understanding the thermal and polymer properties of lignin materials is useful to identify certain applications. Therefore, characterization techniques provide access to essential information for understanding a wide range of materials properties. These techniques reveal phase transition temperatures, structural configurations, physiochemical behaviors, functional groups, and others. Analyses of characterization results serve as basis for identifying potential applications for each variant of lignin product and provide insight into process improvement.

Thermo gravimetric analysis (TGA) utilizes analytical balance to measure the loss of mass under nitrogen or air environment where decomposition, oxidation, and reduction occur, see Figure 2. The physical and chemical properties of the material can be predicted when increasing temperature at a constant rate. TGA also helps determine the composition of material and thermal stability. Loss of water, solvents, decomposition, pyrolysis, weight percent of ash, char and others can be quantified when temperature and time are collected. Furthermore, this method has the capability to perform kinetic analysis where parameters such as activation energy, reaction order, and conversion curves can be predicted. Chapter 2 presents the thermal decomposition of kraft lignin during processing conditions, which is used to predict yields and understand material changes during the preparation of lignin carbon. Differential scanning calorimetry (DSC) is used to detect the glass transition temperature (Tg), which occurs when the amorphous material increases in heat capacity as it changes from glassy-solid to its rubbery state. A difference in Tg is observed between kraft softwood (150 °C) and kraft hardwood (139 °C) as the S lignin in the hardwood favors a more flexible polymer chain. Nevertheless, an identical temperature of decomposition of 273 °C is observed by TGA [18, 19]. Tg measurements can be challenging as the lignin increases in crosslink density, impurity, and condensed structures.

Another characterization method used is gas adsorption, commonly using Nitrogen, in which Brunauer-Emmett-Teller (BET) measures the specific surface area and pore size distribution from a material. The advantage of BET gas adsorption is that it can measure the surface of fine structures. However, the gases of these environments can react with the sample causing inaccurate measurements. A degassing step is used before analysis to remove any undesirable vapor or gas from the surface of lignin carbon. Conveniently outgassing step is performed for a minimum of one hour to a temperature ranging 40 to 70 °C, depending on sample. The technique uses the principle of gas adsorption shown in Figure 3. In theory, the surface area is obtained by the following relationship:

$$S_{BET,total} = \frac{(v_m N s)}{V}$$

$$S_{total} = \frac{S_{BET}}{m}$$

where v_m is the molar monolayer volume of the adsorbent gas, N is the Avogadro's number, S is the adsorption cross section of the adsorbing sample, V is the molar volume of adsorbent gas in equilibrium, m is mass of adsorbent, and S_{total} is the specific surface area. BET has been used for examined the surface changes during thermochemical conversion of activated carbon lignin, carbon fibers, and high ordered carbons [20]. Comparing surface areas during different processing stages can give us indication of how structure changes, and thus what application the material is suitable for.

Chapter 2 includes the study of x-ray powder diffraction (XRD) technique for kraft softwood lignin at different heat treatments to produce lignin carbon. XRD is a technique that helps identify crystalline planes of the material and the unit cell dimension. Also, it allows us to understand the crystallites sizes of the ordered domains within the lignin carbon structure at the carbonization steps. The technique requires simple sample preparation, quick measurement, and can detect mixed phases. Unfortunately it is not useful for single crystals, where sample might need to be grounded in order to see microcrystalline domains.

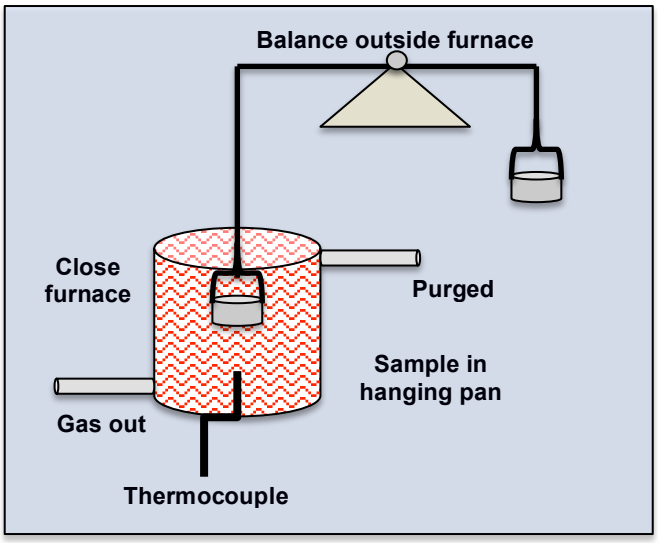

Figure 2. Configuration of TGA in a close furnace. Mass balance is used to measure weight loss from a sample hanged in a pan, while temperature and time are increased.

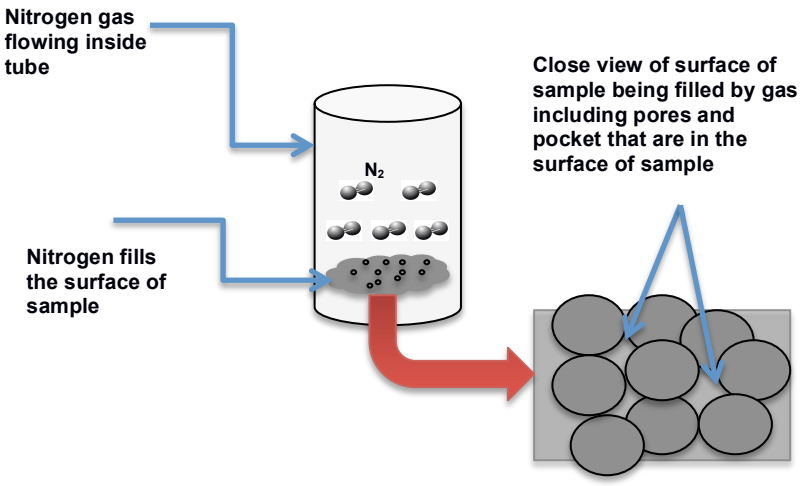

Figure 3. Adsorption measurements where nitrogen gas is introduced after outgas and after nitrogen absorption, pore sizes, and surface areas are estimated via the BET isotherm.

The setup of an XRD experiment is presented in Figure 4a and follows the theory of Bragg's law represented in Figure 4b. In Bragg's law,

$$\lambda = 2d_{hkl} \sin\theta$$

λ is the wavelength (1.5418 Å), d_{hkl} is the lattice spacing, and θ is the Bragg angle of diffraction. William Henry Bragg proposed the equation in 1913, where he found that intensity is produced when crystals produces a specific wavelength and incident angle from the x-ray radiated. X-ray incident on an atom creates an electronic cloud that particularly makes a wave vector of same frequency. The x-ray is generated from the cathode tube were it heats the filament and generates the electrons that target the material. The spectra consist of copper K-α (1.5418 Å) radiation and when is targeted the detector record the signal from scattered x-ray at 2θ angle. The intensity (I_{hkl}) of diffraction peaks is determined by the arrangement of atoms in the entire crystal using the structure factor (F_{hkl}).

$$I_{hkl} \propto |F_{hkl}|^2$$

The total sum of structure factor resulted from scattering atom or material scattered in the unit cell form a diffraction peak from the planes.

$$F_{hkl} = \sum_{j=1}^{m} N_j f_j exp\left[2\pi i(hx_j + ky_j + lz_j)\right]$$

x_j, y_j, and z_j are the fractional coordinates, *hkl* are the atomic planes, and N_j is the fraction of every equivalent position occupied by atom (*j*). Crystallite sizes (τ) can be quantified with Debye-Scherrer equation, which makes use of the peak broadening contribution at the half of the maximum intensity (FWHM), the shape factor (typically 0.9), beam wavelength, and Bragg angle [21].

$$\tau = \frac{K\lambda}{\beta \cos\theta}$$

Elemental analysis is used to determine the content of carbon, hydrogen, nitrogen, and oxygen in lignin, refer to Figure 5. The technique is a quick analysis that helps determine the composition of an unknown and its empirical formula, in this case organic compounds. This technique uses a small amount (about 2–3 mg) of sample material wrapped in a tin foil. For the combustion analysis the material goes to a reactor chamber and with oxygen in excess combustion occurs at a temperature 950 °C. The combustions gases or oxidation a product goes to a chromatographic column or catalytic bed from copper with carrier helium gas, removes excess of oxygen, and nitrogen oxides are reduced to pure nitrogen. Then, when gases passes through a reduction detection occurs for CO_2, N_2, H_2O, and SO_2 with a thermal conductivity detector that gives a signal proportional to the concentration of each element of the mixture. This technique will help us understand the structural composition in lignin carbon at the different processing steps from our resulted carbon product, where the analysis will determine these amounts and a carbon increase is observed during processing.

In Chapter 2 results are presented for KSL materials at the different processing stages to detect amounts of carbon-rich product. Inductively coupled plasma-optical emission spectrometry (ICP-OES) was performed to detect the content of sulfur and other inorganic impurities in KSL that were not detected in elemental CHN analysis. ICP-OES can detect most of the elements from periodic table compared to other elemental analysis techniques. In our case lignin from kraft product contains traceable amounts of sulfur, sodium, and contaminants introduced during processing (e.g., iron) that ICP-OES measures. The technique requires a solution, thus the carbon was broken down into a homogeneous solution composed of hydrofluoric acid (HF), KSL material, nitric acid (HNO_3), hydrochloric acid (HCl), via microwave digestion. ICP-OES detects elements present, mainly metals, and their corresponding concentration. During the ICP stage, a flame is produced from arcing argon and an electromagnetic field ionizes the gas. The intense heat is caused by the inelastic scattering.

An ionization process begins due to inelastic collisions between charged particles and argon gas flowing through the torch. After stabilization, the plasma generated is used to interact with a sample of the material's solution. Charged plasma ions decompose molecules into atoms, which in turn, lose and gain electrons repeatedly. Since each element irradiates characteristic wavelengths, these signals are detected by the optical emission spectrometer. The OES consists of optical chambers that separate the wavelengths generated and photo-detector arrays that identify the atomic composition.

Neutron scattering is one of the most powerful and versatile experimental methods to study the dynamics and structure of a material. It is like to other scattering methods; as it generates an incident beam that interacts with a material to produce scattered signals based on Bragg's relation, refer to Figure 6. In neutron scattering, neutrons interact with the nuclei, thus the neutrons are scattered by the nucleus itself. Neutron scattering experiments measure the number of neutrons scattered by a specimen as a function of wave vector change and neutron energy [22, 23]. Conducting neutron scattering is expensive, costing millions of dollars annually since neutrons are commonly produced by a nuclear reactor or spallation source. Four common neutron scattering techniques are: sample transmission, elastic, quasielastic-inelastic, and spin-echo. Small angle neutron scattering (SANS) is an elastic scattering method used to identify the mesoscale structures and properties of the material. Small angle scattering is defined as

$$\frac{d\sigma}{d\Omega} = \frac{number\ of\ neutrons\ scattered\ through\ angle\ 2\theta\ per\ second\ into\ d\Omega}{number\ of\ incident\ neutrons\ per\ square\ cm\ per\ second}$$

$$\left(\frac{d\sigma}{d\Omega}\right)_{coh} = \sum_{i,j} b_i^{coh} b_j^{coh} e^{i\left(\vec{k} - \vec{k'}\right) * \left(\vec{R_i} - \vec{R_j}\right)} = \sum_{i,j} b_i^{coh} b_j^{coh} e^{i\vec{Q} * \left(\vec{R_i} - \vec{R_j}\right)}$$

a)

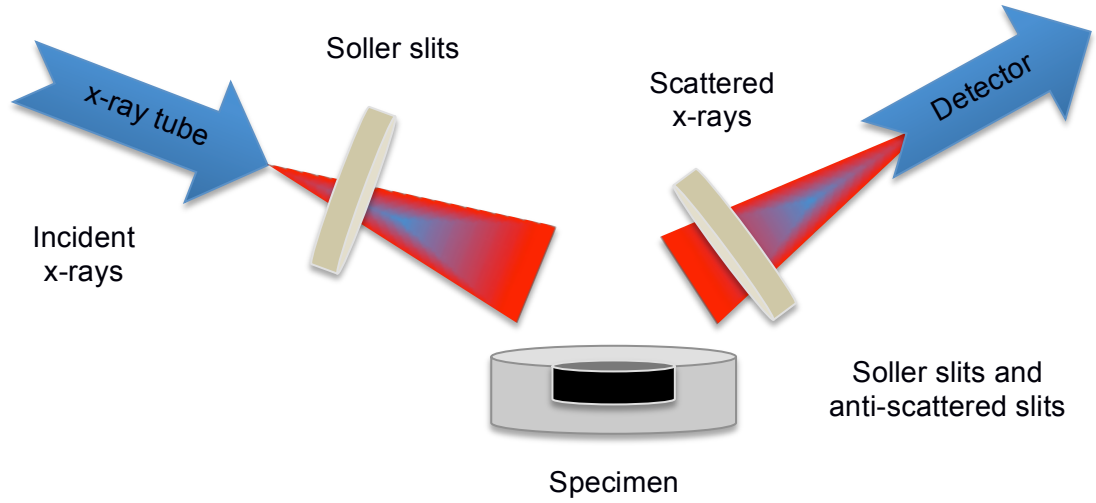

b)

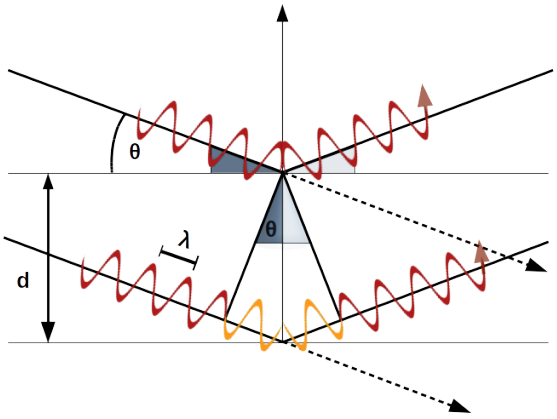

Figure 4. a) X-ray powder diffraction experiment setup demonstrating the incident beam targeting the sample and the resulting scattered rays measured by a detector. b) Theoretical representation of Bragg's law where incident wave vectors interact with surface layers at different depths (*d*) of the crystal structure producing scattered beams. The incident angle (θ) and wavelength (λ) are used to control the detector scanner.

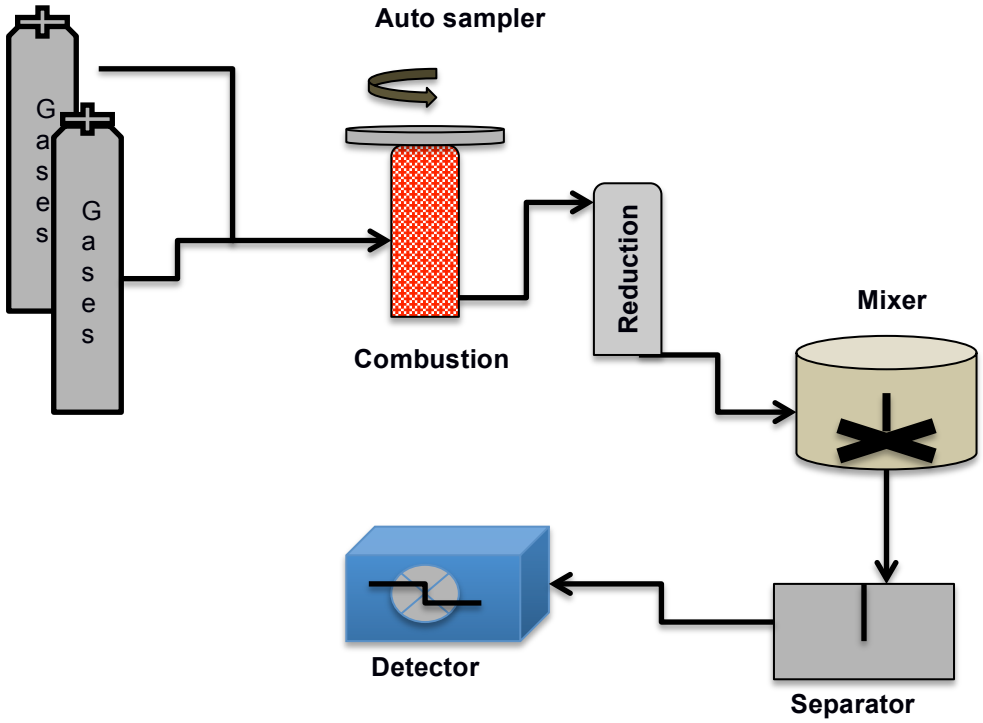

Figure 5. Stages performed during elemental analysis to detect carbon, hydrogen, nitrogen, and oxygen.

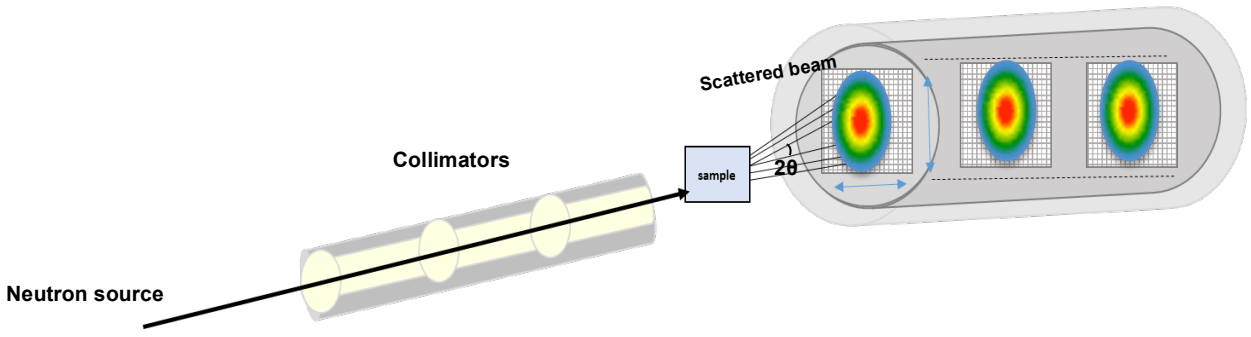

Figure 6. Configuration of a neutron scattering experiment composed of a cold neutron source, collimators, sample, and representation of scattered beam. The collimators define direction of travel of the neutrons. Monochromators are used to allow analysis of the beam energy using Bragg's law.

where the wave vector transfer $\vec{Q}$ is defined by scattering vector, $\vec{Q} = \left(\overrightarrow{k'} - \vec{k}\right)$, see Figure 7. For elastic scattering we have that k' = k, where k is the wave vector of incident neutron, k' is the scattered neutrons, and wavelength is λ.

$$Q = 2k \sin\theta = \frac{4\pi \sin\theta}{\lambda}$$

Generally, SANS covers low Q ranges (0.001 $Å^{-1}$ < Q < 0.5 $Å^{-1}$) and can study both crystalline and amorphous systems [23, 24]. SANS helps understand morphology and is mostly applied to polymers, biomass, colloids and surfactants, soft matter, metals, and other solids and liquid materials.

Particularly, SANS can be helpful to deduce material information at atomic level or nanometer levels. SANS is sensitive to hydrogen and deuterium isotopes, and to light elements, such as hydrogen, carbon, and nitrogen. Material structures can have identical conformations but different scattering lengths, and may produce coherent scattering. In such cases, a contrast matching technique, where hydrogen is replaced with deuterium, is used to produce different elastic scattering in order to correctly measure the structure components. In simple words to allow each phase or component in the material generate different scattered beams; this helps distinguish among the lignin structure. In elastic scattering the energy of the incident beam is small relative to the ionization energy of the atom, thus the beam does not displace atomic electrons but changes direction, and energy is conserved.

Another important factor for SANS analysis is the concept of scattering invariance at low Q limits; Andre Guinier established this relationship [23]. The Guinier approximation,

$$\ln\big(I(Q)\big) = \ln\big(I(0)\big) - \frac{R_g^2}{3}Q^2$$

relates the scattering intensity (I) based on the radius of gyration (R_g) and scattering vector. The radius of gyration describes the size of the particles since it estimates the

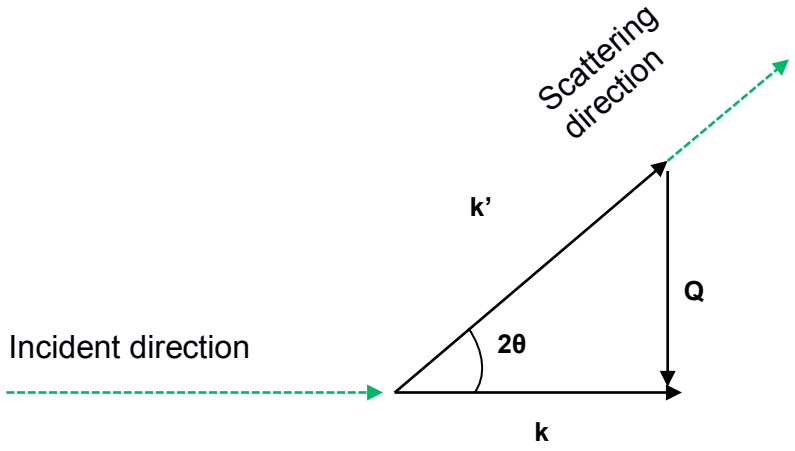

Figure 7. Geometrical representation of incident and scattered beams during SANS experiments.

distribution of components around a particle's axis based on its geometry. For example, for spherical particles of radius *R*

$$R_g = \sqrt{\frac{3}{5}}R$$

If we have an ellipsoid $\mathrm{R_g} = \frac{R}{\sqrt{2}}$ and for a solid rod $\mathrm{R_g} = \sqrt{\frac{R^2}{2} + \frac{L^2}{12}}$ where *L* is the length of the rod and *R* is the rod radius. Guinier approximations and contrast matching provide a roadmap for analysis where you can approximate information of particle size, shape, and composition [23].

PROCESSING LIGNIN BASED CARBON

Graphite in the global market

The aromatic structure and high carbon content in lignin lets one believe that it is suitable for developing graphitic materials. A recent study in 2016 shows graphite consumption of 24,200 tons by U.S firms valued at $25.6 million. Most of mineral

graphite used in the US is imported (39,500 tons) [25]. In 2016, China remained the world's largest producer of natural graphite with 780,000 tons from a total global production of 1,200,000 tons. Figure 8 shows commercial demand of graphite has generally increased since 2000. For this reason, the US government stimulates domestic research for natural and synthetic graphite substitutes due to its increase demand, national security, and competitiveness [26]. Graphite can be found in three types: vein, flake, and microcrystalline or amorphous. Vein graphite is found in fissures of "ore" rocks that are created by subterranean formations compacting graphitic carbon. Flake graphite has a lamellar structure and is found in metamorphic rock, each flake is crystallized and separated individual. Amorphous graphite is found as small fragments in metamorphic rock [27]. Globally graphite is used for a whole host of applications, for example, for brake linings, pencils, lubricants, refractory materials, steel industries, foundry operations, electronics, and carbon-based composites. Currently the fastest growing application of graphite is for electrochemical storage. The graphite market is shifting from amorphous natural graphite towards flake and synthetic ones. Today 65% of natural graphite is mostly used for batteries and around 30% of synthetic graphite is used for this application. The natural flake graphite is 80 to 98% carbon and is the most anisotropic between other graphite forms. Flake graphite has desirable properties in terms of size (mesh), softness, high heat conductivity, and high heat resistance. Large flakes tend to be of high purity grade graphite, which enhances the efficiency of typical battery anodes [28]. An high increase in demand for lithium ion technologies for energy storage is projected for the upcoming decade, mainly because of the interest in mass adoption of electric vehicles, grid storage, and related applications.

Carbon structure

Graphite is a parallel stacking of 2D carbon layers as a result of carbons with sp^2 hybrid bonding in aromatic rings. It occurs in vein, flake, or amorphous variants. Figure 9 shows the crystallographic stacking of the form ABAB for a hexagonal system. However, turbostratic structure in carbon occurs with random stacking of layers as a result of translation and rotation displacements. X-ray powder diffraction analysis of

graphite material indicates a strong anisotropic structure with *00l*, *hk0*, and *hkl* index groups.

Graphitic carbon materials are attractive due to their electromagnetic properties and high thermal stability, see Figure 10. Characterization studies indicate lignin based carbon materials form very small graphitic crystals, but have a high degree of crystallinity [30]. In composite and polycrystalline materials, hierarchical structures represent the continuous multi-scale decomposition of small particles, particle matrices, and matrix stacks [31]. Understanding the structure-property relationships at each hierarchy level is key for manipulating the material to have desired characteristics.

Analytical models designed with a hierarchical approach have been used to interpret scattering data of lignin-based carbon composites in order to predict structural phases at the atomic and meso- scales [33]. Li studied the structure and thermal stability properties during thermostabilization and carbonization of soda (or sulfur-free) lignin [34]. Carbon composition from soda lignin varied with pyrolysis temperature. At temperatures below 260 °C, oxygenated structure increased due to oxidation of aliphatic moieties, at temperatures between 260–290 °C, condensation of aromatic rings increased due to reaction of carboxyl groups, and at temperatures above 290 °C, oxygenated structures decreased and C-C aromatic structure increased. The carbonization stage converts carbon structure to hard-graphitized materials and reduces oxygen and other thermolabile elements such as sulfur and nitrogen. During pyrolysis C-C bonds, which link the precursors' aromatic rings, break and become saturated alkyls. Also, the formation of polycyclic aromatic carbon and coke formations begins, as well as CO gas significantly increases [35]. At temperatures above 600 °C oxygen and hydrogen is released as CO_2, CO, and CH_4. The formation of polycyclic aromatic hydrocarbons continues to increase in the structure along with the presence of stable phenols. Above 800 °C, H_2 becomes the main gas released due to polycondensation of aromatics as well as amounts of O, N, and S [35].

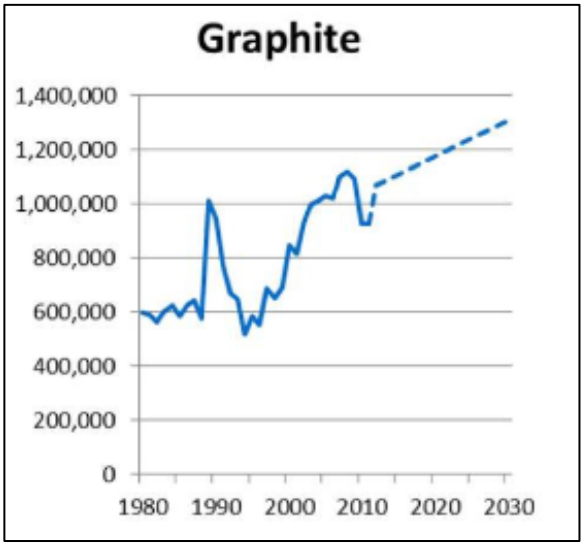

Figure 8. Total global mined graphite between 1980 and 2011. Projected graphite demands assuming linear trends for recent and future years [29].

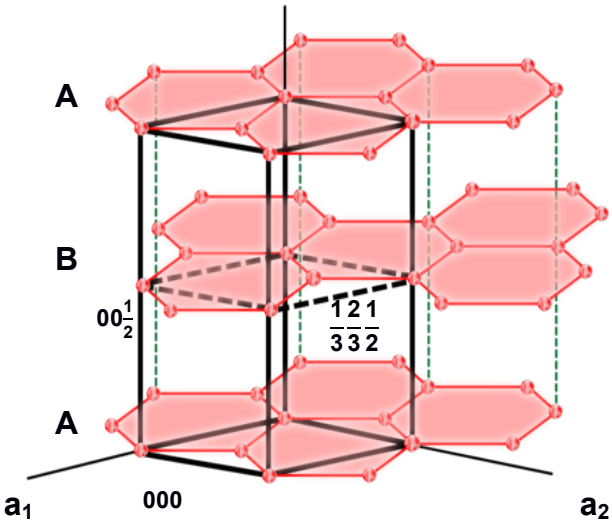

Figure 9. Unit cell representation of hexagonal graphite and crystallographic coordinates [32].

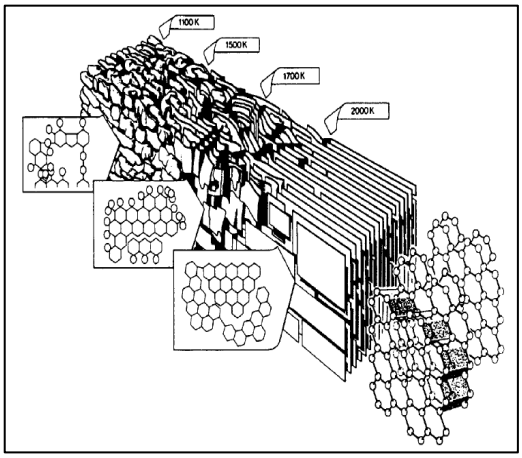

Figure 10. Structural model of graphite during carbonization process showing that increase in temperature promotes graphitic ordering and crystal growth [36].

CHARACTERIZATION OF LIGNIN CARBONS

Raman scattering is a non-destructive and inelastic scattering technique, where molecules in the sample absorb a high-energy incident beam of photons. An effect of the high-energy beam is that it changes atomic electrons from current orbital levels, making the scattered beam dependent on these energy level transitions. The inelastic scattered beams correspond to the energy needed to excite a molecule to higher energy state, thus information of the dynamics of molecules is made available. Specific elements and structural configurations generate unique inelastic scattering patterns that help identify characteristic peaks (order and disorder peaks).

A Raman spectrometer uses a powerful laser source of visible, monochromatic radiation. The setup consists of a laser source, illumination system (microscope), and spectrometer as shown in Figure 11. Samples are irradiated at an angle of 90°, then the intensity of the scattered beam is detected and measured in the infrared spectra. It is important to note that Raman shifts are independent of the wavelength of excitation, making it a versatile method. The main scattering types of Raman emitted radiations are: Stokes, anti-Stokes, and Rayleigh. A detailed study of lignin carbon fibers using Raman scattering is presented in Chapter 3. The spectra of processed hardwood and grass lignin show the characteristic D and G bands associated with graphitic structures, although intensity and peak shifts differ. The D band is associated with disordering and

G band with ordering of the structure. Peak band positions, intensity measures, and intensity ratios give insight to the amount of ordered or disordered structures [37]. The shift of the peaks are related to structural stresses, intensity variations depend on the amount of material corresponding to a specific peak band, and peak width is associated with crystallinity.

APPLICATIONS

Carbon materials have many potential applications in areas related to electrode design, catalysis support, capacitors, adsorbents, and others. The development of lithium-ion batteries has increased since 1970 where lithium metal was used as an anode with high capacity and energy density.

Graphitic carbon was found to be stable for lithium insertion and extraction. Theoretical discharge capacity of graphite is 372 mAh g^{-1} [38, 39], one lithium per six carbons. These materials are commercially advanced, but understanding of its electrochemistry process is still continuously evolving. The electrolyte is mainly used to transport the Li-ions between cathode and anode.

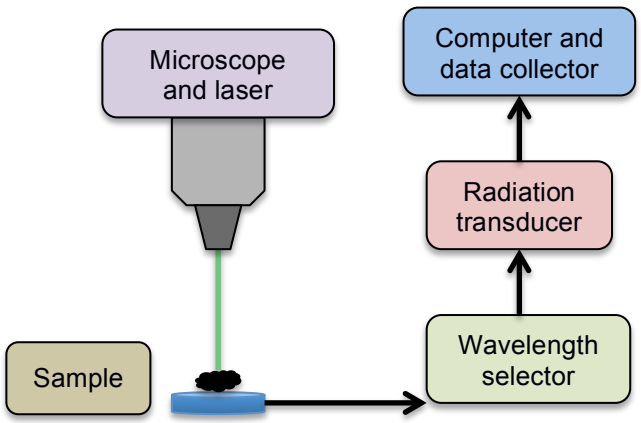

Figure 11. Flow diagram of a Raman scattering experiment.

However, electrolyte decomposes in the graphite surface during battery operation, but a complete decomposition does not occur due to the formation of a solid electrolyte interface, where electrochemical processes are thermodynamically unstable but kinetically protected [39].

Exhaustive and reliable characterization of lignin at the structural and chemical levels is valuable in understanding the array of lignin-based products that can be developed. Energy storage materials are increasingly important as the fraction of US energy is derived from fluctuating renewable sources (i.e. solar and wind) increases. Li-ion batteries will continue to play a role in short- and long- term energy storage for transportation, device applications, and potentially for grid storage. Lowering the costs of key battery components is crucial for adoption. A cost model for Li-ion pouch cells estimates the cost of each battery component: anode graphite ($9/lb), PVDF binder ($5.5/lb), NMP solvent ($1.25/L), carbon black additive ($2.5/lb), copper foil ($7.5/lb), separator ($3/$m^2$), electrolyte ($22/L), and cathode ($19/lb) [40]. Additionally, the study provides a detailed cost breakdown of manufacturing these batteries. Today, battery anodes are manufactured from mined and processed graphite. Economic and environmental alternatives to graphite anodes can be derived from lignin-based carbon composites. Another study took advantage of lignin's natural abundance and converted it into high-grade carbon composites suitable for battery electrodes. That work demonstrated how carbon fibers derived from hardwood lignin could achieve performance levels on par with flake graphite in lithium-ion battery anodes [41, 42].

Polyacrylonitrile (PAN) is commonly used as a polymeric precursor for carbon fibers. Engineering materials in the automotive and aerospace industry use carbon fiber reinforced polymers to substantially reduce the weight of components. Because carbon fibers have a high strength-to weight ratio, carbon fiber composites replacements for steel parts improve fuel efficiency and reduce gas emissions. Efforts to use lignin as an economical renewable resource for carbon fiber production are carried out. Nevertheless, the branched and irregular structures found in lignin tend to produce lower quality carbon fibers when compared to PAN as it produces a less ordered carbon structure. This same structure may prove to be key to increasing the energy storage capacity of lignin based carbon over graphite.

MOTIVATION AND OBJECTIVES

Graphite is an attractive material due to its electrical and thermal conductivity, in addition to being highly stable at high temperatures. Nonetheless, graphite is not a domestic resource. Lignin contains a high concentration of carbon content making it suitable for producing domestic graphitic carbon materials. Electrochemical storage applications and vehicular industries are examples of industries that can clearly benefit from a cheap and domestic source of lignin based carbon materials. This work addresses the processing-structure-property relationships of different lignin sources, kraft softwood, organosolv switchgrass, and organosolv hardwood, and processing conditions. The main goal is to synthesize in-house materials from these renewable sources to serve as substitutes for mineral and fossil derived carbon-based materials.

Chapter 2 focuses on the role of unit operations during the carbonization process of kraft softwood lignin, and its resulting impact on materials structure and performance in an electrochemical cell. The principal objective is to establish relationships between degrees of graphitization of the lignin carbon product, as temperature and duration were varied during pyrolysis and reduction stages. Characterization of crystal size, surface area, and elemental composition are used to deduce such relationships. In addition, the electrochemical properties of lignin carbon material were investigated when used as the anode in lithium-ion coin cells.

The focus in Chapter 3 is to characterize carbonized lignin fibers from switchgrass and hardwood feedstock to measure ordered and disordered structures, and to understand how the choice of feedstock impacts the processing-property-structure relationship. Small angle neutron scattering experiments were conducted to visualize pore defects, surface shape, and crystallite aggregates within both green and carbonized fiber structures. Contrast variation was used to resolve pore structure and particle sizes using different solvents. Raman scattering on lignin carbon fibers was used to identify the degree of graphitization, this includes the order and disorder peaks, and crystallite sizes. Results were compared to understand structural changes from the two types of lignin sources, which vary in monomeric units.

CHAPTER 2

PROCESSING-STRUCTURE-PROPERTY RELATIONSHIPS FOR LIGNIN-BASED CARBONACEOUS MATERIALS USED IN ENERGY STORAGE APPLICATIONS

ABSTRACT

Lignin, an abundant organic polymer and a byproduct of pulp and biofuel production, has potential applications due to its high carbon content and aromatic structure. Processing-structure relationships are difficult to predict due to lignin's heterogeneity. The work discusses the role of unit operations in the carbonization process of softwood lignin, and its resulting impact on materials structure and electrochemical properties when used as the anode in lithium-ion cells. The processing variables include the presence, temperature, and duration of thermal stabilization, pyrolysis, and reduction. Materials are characterized at the atomic- and micro-scales. High temperature carbonization, 2000 °C, produced larger graphitic domains than 1050 °C but resulted in reduced capacity. Coulombic efficiencies over 98% were achieved for extended galvanostatic cycling. Consequently, a properly designed carbonization process for lignin is well suited to generating low-cost, high-efficiency electrodes.

INTRODUCTION

Advances in materials processing have led to the conversion of wood pulp into a variety of new lignin-based products and substitutes such as carbon fibers and organic polymers [43, 44]. Lignin is commercially available as a byproduct of paper production and potentially cellulosic bioethanol production in the near future. The kraft process produces 130 million tons of pulp per year making it the most widely used process in the world for producing pulp and paper production [45]. The majority of the pulping waste is burned for process heat, yet 34 million tons of residual lignin is estimated to remain [46]. This pulping method is extremely versatile as it can produce very high strength pulps from softwoods. Unfortunately, the residual lignin precipitated from kraft black liquor contains many inorganic (1–2%) and organic contaminants, most notably 1–2% sulfur

(S) and sodium (Na) [2]. Kraft lignin's contaminants and the heterogeneous, random, and condensed structure of the precipitated molecule make it undesirable for many applications. Nevertheless, this also makes kraft lignin a high-volume low-cost source of carbon. Recent work has demonstrated promise in producing electrodes from a higher cost organosolv lignin that has high reversibility [47]. We are attempting to take advantage of the sulfur contaminants [48] along with the amorphous carbon (C) structure of lignin [42] to achieve high capacity and reversibility [49] in battery electrodes.

Lignin refers to a class of aromatic polymers found in wood cells, mainly in vascular plants, such as trees and grasses. Along with hemicellulose and cellulose, lignin polymers are one of the core constituents in the dry mass of wood and contain a high carbon concentration. The amorphous and cross-linked three-dimensional structures of lignin make it a complex macromolecule to fully understand. These structures result from the oxidative binding of monolignol precursors that create syringyl (S), guaiacyl (G), and *p*-hydroxyphenyl (H) units (Figure 12) [50]. In general, trees can be categorized into hardwood (angiosperm) and softwood (gymnosperm) species, both of which contain lignin, though the molecular weight, structure and chemical content vary from species to species. Specifically, softwood lignin is almost exclusively composed of G units, and hardwood lignin contains varying amounts of mostly S units, lesser amounts of G units, and less frequently H units. H units are found in more abundance lignin from herbaceous crops such as perennial grasses and annual agriculture crops.

In this work, we investigate the potential use of the residual lignin precipitated from kraft softwood black liquor (Indulin AT, MeadeWestvaco). In the adoption of a new material in any industry, it is essential to establish the processing-structure-property-performance relationships. The processing conditions control the structure of the material at the atomic-, meso- and micro-scales. Since this structure dictates material properties, investigation of the processing-structure-property relationships may lead to high performance devices that include lignin-based materials with targeted properties.

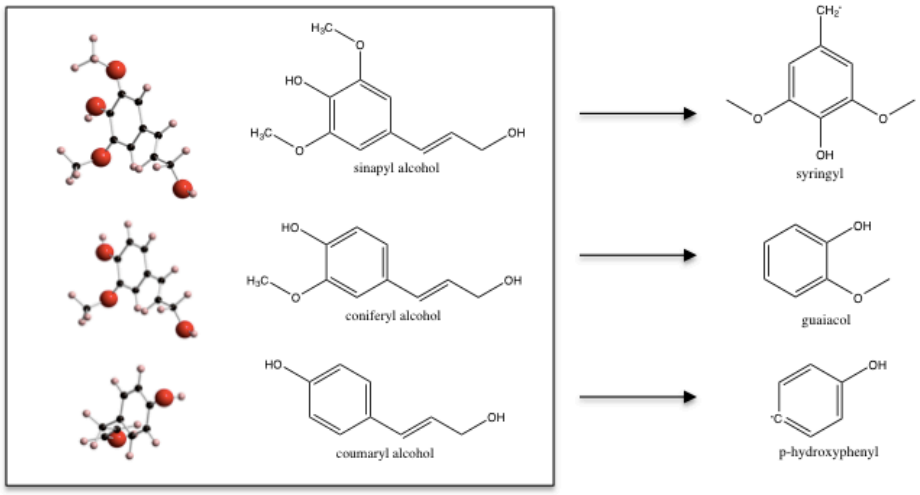

Figure 12. The three principal lignin precursors synthesized from monolignol-pathways are synapyl, coniferyl and *p*-coumaryl alcohols. These cross-link with lignin polymers to form syringyl, guaiacyl, and *p*-hydroxyphenyl units [51]. During kraft processing, these units undergo structural changes enabling a thermally stable lignin with complex carbon-carbon linkages.

An in-depth study of kraft lignin activated carbons, including analysis of surface area, thermodynamics and kinetics, indicates that adsorption in the processed material is both endothermic and spontaneous [52]. Another study shows the effects of fast pyrolysis on physical and chemical properties, such as composition, ash content and water content, for three types of lignin, which included Indulin AT [53]. Initially thought to be a contaminant, the presence of sulfur in kraft softwood lignin (KSL) has been investigated as a potentially beneficial, naturally occurring dopant [48].

Specific to this work, we explore the effects of processing conditions in the conversion of the residual lignin into a high-grade, hierarchically structured carbon composite with applications in the energy storage and environmental remediation industries. Previous work presents how carbon composite electrodes for ion storage have been manufactured from this material [47, 49, 54]. Carbon composite materials result with crystalline (graphitic) and amorphous domains. This work has shown that processing conditions, such as the pyrolysis temperature and rate, of the residual lignin can have a drastic impact on the structure of the resulting material, including the volume fraction of the graphitic domain and the size of the graphitic crystallites. Molecular simulation has mapped experimental neutron scattering data of a hardwood lignin into

atomistic structures as a function of pyrolysis temperature [42]. Computational approaches have been used to understand processing-structure relationships of amorphous graphite from scattering data analysis [33]. Because of the unique structure and composition of these carbon composites, lignin-carbon composites can achieve capacities on par with the theoretical lithium-ion (Li-ion) capacity of graphite (372 mAh g^{-1}) while maintaining excellent reversibility and long cyclability in Li-ion battery electrodes [47, 55]. Presently, natural graphite is mined where the largest producer is China with an estimated worldwide production of 66% in 2015. Several industries drive graphite production and the demand for Li-ion batteries, fuel cells, electric vehicles and grid storage are becoming key factors in increasing graphite production [28]. An advantage of our lignin-based graphite processing is that it is synthesized from waste products from kraft processing which is the main technique in the paper industry.

The objective of this work is to more fully explore producing energy storage materials based on a low-cost, renewable source of carbon, lignin. There are two hypotheses in this work. The first hypothesis states that careful selection of processing conditions provides sensitive control over the surface area, the porosity, the volume fraction and size of crystalline domains, and other structural factors. The second hypothesis is that the structural differences induced by processing dictate the performance of carbon anodes in battery applications. Thus, we examined the role of unit operations in the carbonization process of lignin, and its resulting impact on materials structure and electrochemical properties. Processing parameters under investigation include the temperature, gas environment, and duration of thermal stabilization, pyrolysis, and reduction steps.

METHODS

Processing of lignin powder

The dry kraft lignin powder is exposed through a series of heat and processing treatments for making a highly graphitic structure (Figure 13a). The heating steps include thermal stabilization, pyrolysis, and reduction. Collectively, these three steps result in a process referred to as carbonization. In this work, thermal stabilization is combined as a pre-step during pyrolysis, thus reducing processing time. A tube furnace

(Thermo Scientific Lindberg Blue M model) setup with inert gas conditions contains the KSL powder on a ceramic crucible (Figure 13b). During carbonization, KSL material undergoes an irreversible phase change and produces a richer carbon content material also known as char. The thermal stabilization step increases oxygen (O) and carbon contents while decreases hydrogen (H_2). Carbon content continues to increase throughout pyrolysis treatment. Finally, reduction stabilizes the material with the introduction of hydrogen.

First, KSL powder is exposed to nitrogen (N_2) with water vapor (H_2O), in a tube furnace for thermal stabilization and pyrolysis. The inert gas, N_2, passes through a bubbler at room temperature and feeds into the furnace at a volumetric flow rate of 3 L min^{-1}. During the thermal stabilization and pyrolysis step, the furnace is heated from 30 to 1000 °C at a rate of 10 °C min^{-1} and then held at 1000 °C for one hour. Thermochemical decomposition of the organic material starts at approximately 200 °C. The effluent gases, which include steam, nitric oxide (NO), carbon monoxide (CO), carbon dioxide (CO_2) and sulfur oxides (SO_x), are released from the system and trapped for odor control. To increase surface area and improve resulting structure, the char is broken up into smaller pieces in two steps. First, the char is grounded into a micro powder with a blender for five minutes. Second, the material is milled with a planetary ball mill (PM100 RETSCH model), resulting in particle sizes in the nanometer range. The ball-milling process uses a stainless steel grinding container with a mixture of 2 and 10 mm diameter stainless steel balls. One-third of the container was filled with sample and grounded at 350 revolutions per minute (rpm) for three hours, composed of alternating 15 minute periods of ball milling and holds at ambient temperature for cooling. After ball milling, the material is sieved to separate the grinding balls from carbon material. The furnace is setup with an argon-hydrogen (Ar-H_2) gas mixture (3 L min^{-1}) for the reduction step. Reduction is conducted at temperatures of 1050 and 2000 °C, with a heating rate of 10 °C min^{-1} and one hour hold.

a)

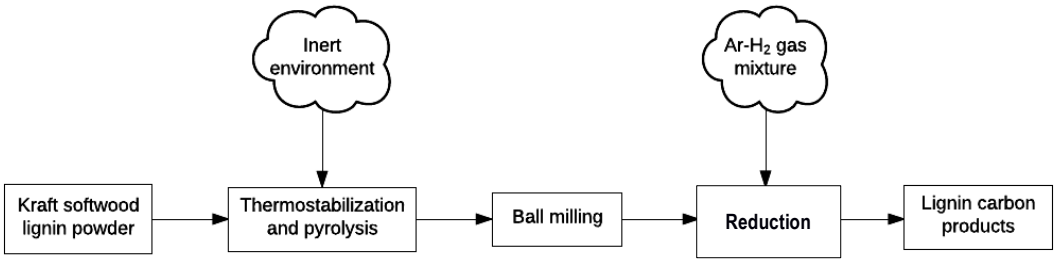

b)

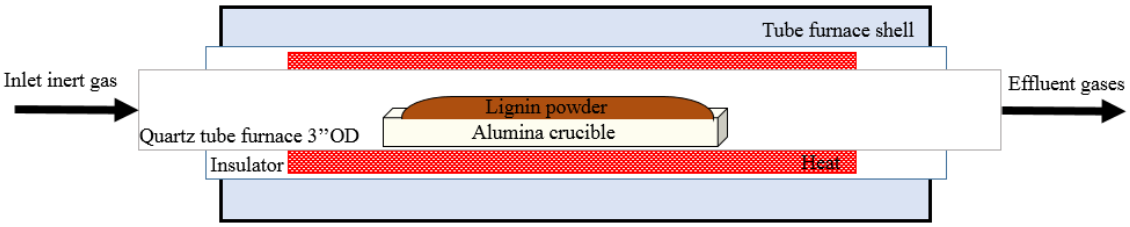

Figure 13. (a) Flow diagram of heat and processing operations during lignin carbonization. First, the raw lignin powder is treated in a combined thermal stabilization and pyrolysis step under an inert gas environment. The material is ball milled to reduce particle size, followed by a reduction heating step under an Ar-H_2 environment. (b) Furnace setup of a cylindrical quartz crystal tube used for both heat treatments applied to the KSL powder. The lignin material rests on an alumina crucible, gas mixtures are input into the tube, and effluent gases are released during heat treatments.

Characterization techniques

Scanning electron microscopy and particle size analysis

A scanning electron microscope (SEM), model HITACHI TM 3000, was used to collect micrographs of carbonized material. The SEM micrographs were collected with backscatter composition signal at 5.0 kV and 1650 mA. Specific details of individual micrographs, such as magnification, scale, and working distance, can be found in result section. Subsequently, ImageJ software [56] was used to measure particle sizes before and after ball-milling procedure. Particle size homogeneity is essential for high surface area when material is used for anode electrodes. Performance of these electrodes is directly affected by particle uniformity in contact surfaces.

X-ray diffraction

In order to identify the degree of crystallinity in the processed lignin carbon, x-ray diffraction (XRD) scans were performed at room temperature using a PANalytical Empyrean diffractometer. XRD scans with Cu-kα (λ = 0.154 nm) ranged from 5 to 115 two theta degrees with a continuous step size of 0.013 at 45 kV and 40 mA. Using Highscore Plus software [19], the scanned data was refined based on peak fitting to obtain the full-width at half-maximum and the interlayer spacing (or d-spacing). The crystal size was determined using the Debye-Scherrer equation [21]. Crystallographic planes (hkl) were indexed for a graphite standard pattern based on carbon graphite with a hexagonal structure, i.e., a non-cubic system.

Elemental analysis

The Perkin Elmer 2400 Series CHNS/O analyzer was used in CHN mode to determine the weight percent of C, H_2, and N_2 from our lignin-carbon products. In principle, CHN utilizes an oxygen environment for combustion at 925 °C and a helium environment for reduction, separation, and detection. Sample with weights ranging from 1.5 to 2.5 mg were measured in a tin foil. Acetanilide was used as the standard to calibrate the instrument. Samples are automatically injected into the system and, when combustion is reached and reduced, CO_2, N_2, H_2O, and SO_2 gases are formed. For every run, gases in the control chamber are controlled by pressure, temperature, and

volume. Once homogeneity is achieved in the product gases, the CHNS/O analyzer detects the contents of N_2, CO_x, and H_2O.

ICP analysis

S and Na contents in both KSL and carbonized material were determined with inductively coupled plasma-optical emission spectroscopy (ICP-OES). The samples prepared had mass of 0.10 g. The carbon material was mixed with 10 mL of nitric acid (HNO_3) (67–70%), 3 mL of hydrochloric acid (HCl) (34–47%), and 0.4 mL of hydrogen fluoride (HF) (47–51%) followed by dissolution in a microwave digester to achieve a homogenous solution. The microwave settings consisted of a 40 minute ramp reaching around 200 °C and held for one hour. The solution was cooled to room temperature and this cycle was repeated three times. Then, the HF in the solution was neutralized with 5 mL of boric acid (H_3BO_3) (4%) during the final cool down. Next, solution was diluted with distilled water and centrifuged for 30 minutes at 9500 rpm. Diluted samples were set up for ICP analyses in an auto sample tray where data was collected.

Thermogravimetric analysis

Thermogravimetric analysis (TGA) was performed with a Perkin Elmer Pyris 1 in order to detect mass changes due to the pyrolysis and reduction steps. TGA allows understanding decomposition and thermal stability of KSL by monitoring thermal degradation via weight loss with respect to temperature. Depending on the material, the extent of thermal degradation will vary and is characterized by a temperature at which the maximum weight change occurs [57]. Also, heat treatment conditions play an important role on the thermodynamics and kinetics of the thermal decomposition[58]. This technique also provides the char and ash content. For the raw KSL material, the test was performed in inert atmosphere from 30 to 925 °C at a rate of 10 °C min^{-1}. When the test achieved a temperature of 925 °C, the inert gas is switched to an air environment. For the pyrolyzed and reduced materials, TGA was performed in an inert environment from 30 to 1000 °C at a rate of 10 °C min^{-1}.

BET analysis

A Beckman Coulter SA 3100 was used for Brunauer-Emmett-Teller (BET) analysis in a nitrogen environment to measure the specific surface area and total pore volume of the lignin carbon. BET analysis helps predict the performance of the processed material by providing insight into its porosity. This technique uses the Langmuir adsorption model and applied multilayered gas molecule adsorption. The gas molecules adsorb on the solid particles with no interaction between adsorbates. Prior to the BET measurements, the materials underwent outgassing for two hours at 180 °C under high vacuum to remove adsorbed species.

Half-cell preparation

Slurry carbon preparation and coating

Lignin slurries were prepared by mixing the KSL carbonized powders with poly(vinylidene difluoride) (PVDF) binder (9300, Kureha America) and conductive carbon additives (C-NERGY Super C65, Imerys Graphite & Carbon) in a mass ratio of 83:15:2, respectively. Anhydrous N-methyl pyrrolidinone (NMP, Sigma-Aldrich) was used as the solvent. The slurry was mixed in a high shear rate SPEX mill for one hour. The slurry was tape casted (or wet coated) on a copper current collector with a doctor blade of 2 and 3 mil gap. The coating was dried at room temperature with less than 1 ppm of moisture content. Electrodes of 13 mm diameter were punch pressed from the coating with nominal loadings of 2–5 mg cm^{-2} (Figure 14a). Afterwards, prior to cell assembly, the punched electrodes were further dried overnight in vacuum chamber at 80 °C.

Cell assembly

The dried electrodes were fully assembled into 2032 standard coin cells of 20 mm diameter and 3.12 mm thick. Assembling was performed inside a glove box filled with argon and moisture content less than 1 ppm. The KSL carbonized powder at 1050 °C was used to build two half-cell batches, i.e., with and without ball-milling procedure. An additional half-cell batch was assembled with the ball-milled carbonized powder at 2000 °C. Figure 14b shows the configuration followed for the coin cells with ball-milled

carbon anode, while Figure 14c corresponds to the coin cells with non-ball-milled carbon anode. Standard Li-ion battery grade electrolyte (PuriEL from soulbrain MI) consisted of 1.2 M $LiPF_6$ in ethylene carbonate/dimethyl carbonate (3:7 wt/wt). Celgrad 2325 microporous trilayer membranes of 16 mm diameter served as separators. The Li metal (Alfa Aesar) used was 0.75 mm thick and functioned as the counter electrode [59]. The results section provides performance comparisons of both assembly methods.

Electrochemical experiment parameters

Electrochemical performance was characterized for Li-ion half-cells with lignin-carbon anodes. Cells made with inhomogeneous lignin powder (not ball-milled) were tested with galvanostatic charge and discharge cycling on a MACCOR battery cell tester. The cutoff voltage window was 5 mV and either 1.2 or 2 V at a current density of 30 and 24 mA g^{-1}, respectively. A potentiostatic step was incorporated during lithiation (at 5 mV), with a 5 µA cutoff threshold. The cells made with finely processed lignin powder (ball-milled) were cycled from 5 mV to 1.5 V on a VSP Bio-Logic potentiostat-galvanostat. A potentiostatic step was incorporated during lithiation (at 5 mV), with a 5 µA cutoff threshold.

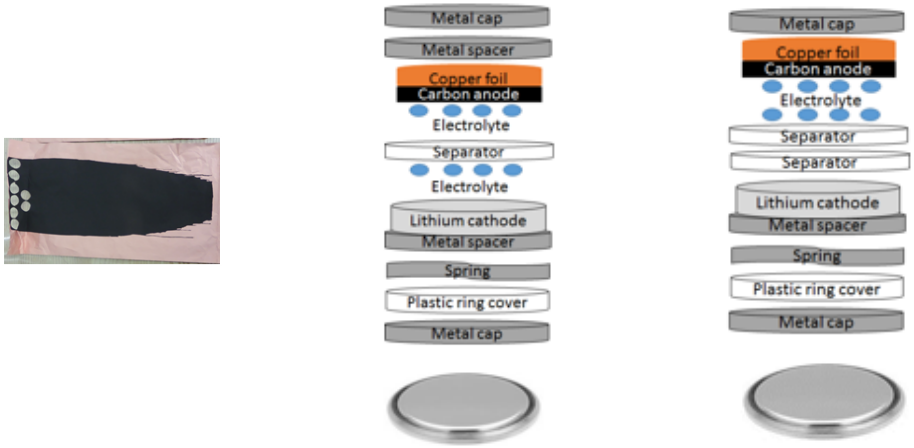

Figure 14. Components and configuration of 2032 standard coin half-cells using ball-milled and non-ball-milled KSL carbonized powder anodes: (a) Anode electrodes were punch pressed from a dried slurry carbon coating; (b) Assembly diagram of coin cells using the ball-milled carbon anode; (c) Assembly diagram of coin cells using the non-ball-milled carbon anode.

Current densities ranging from 7.5 mA g^{-1} to 750 mA g^{-1} were run incrementally every five cycles.

RESULTS AND DISCUSSION

Two major topics are discussed in this section 1) structural changes that occurred in the kraft softwood lignin material as a result of pyrolysis and reduction, and 2) electrochemical characterization of the material properties corresponding to the changes induced by the various processing conditions.

Processing-structure relationships

Physical characterization

We begin the structural analysis with physical characterization of the pyrolyzed KSL material. The primary processing step that impacts particle size is the ball-milling step. In Figure 15, SEM micrographs are presented characterizing the particle size before and after ball milling. Microstructure distortion and graphitic rearrangement are structural defects influenced by ball milling. The particle sizes were approximately 10–40 μm prior to the ball-milling procedure. The particle size was reduced to a range between 0.6–2 μm after one hour of ball milling. An additional two hours of ball milling further reduced the particle size to 64–178 nm. These results show a particle size reduction of two orders of magnitude and greater particle homogeneity in the KSL material after the completion of ball milling. Particle size plays an important role in accessing anode capacity and determining the initial irreversible capacity loss which is discussed in coin cell performance [39]. Particle size is closely coupled with surface area. However, whereas ball milling is the process largely responsible for particle size, the reduction step is assumed to be the critical processing step for control of surface area. In Table 1, the results of a BET analysis of the reduced KSL material are presented as a function of reduction temperature. In all cases, the material was held at the reduction temperature for one hour in an Ar-H_2 mixture. Nominal difference in the BET surface area and pore volume was observed for reduction temperatures of 1050 and 2000 °C, and corresponding sample masses of 0.112 and 0.114 g. These reported

values in the range of 70–80 m^2 g^{-1} are comparable to kraft lignin materials reported in literature [20, 60].

Characterization of composition

In order to characterize the composition of the material, we employed three techniques: elemental analysis (C, H, and N), ICP (S and Na) and TGA (char and ash content). The elemental analysis results are summarized in Table 2. These analyses were performed across the entire process from the raw KSL material to several reduced materials. The carbon content of KSL, which starts at 61%, continues to increase during processing. The KSL shows 79% C after pyrolysis and between 88–95% C after reduction, depending upon the reduction temperature. During the process, the amount of hydrogen commensurately decreases from an initial 5 to 0.05% after reduction at 1050 °C. We note that reduction in the presence of H_2 does not serve to increase the H_2 content in the KSL material. Other tests performed showed that the measured surface area is a function of the outgassing time. The amount of nitrogen, initially less than 1%, always remains less than 1%. The oxygen content is not directly measured in the elemental analysis. However, since the rise in C is greater than the loss of any other component, we can infer a loss in O, which gives rise to the generation of H_2O, NO, CO, CO_2, and SO_x in the effluent gases.

The ICP analysis results are summarized in Table 3 for the raw KSL and reduced materials. The experimental results show the presence of sulfur and sodium content as expected from the kraft process. In any case, the S and Na contents are nominally no more than 2.2%. According to literature, S presence might improve graphitic structure of KSL by allowing stronger intermolecular cross-linkages during dehydrogenation process [51]. The iron (Fe) content was characterized after ball milling. Therefore, we suspect that Fe is a contaminant from the stainless steel balls used in ball milling. Some of the samples were not completely soluble in the solution used for ICP treatment, even after three rounds in the microwave digester. Insoluble carbon contents, with an average mass of 0.4 mg, are assumed to remain after drying the material. The insoluble mass was subtracted when normalizing the element contents as shown in Table 3.

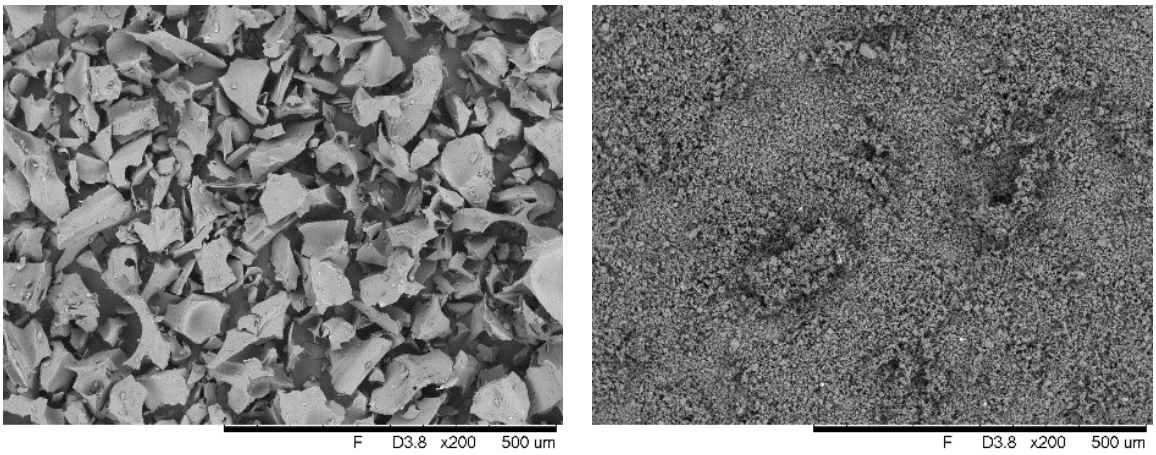

(**a**) (**b**)

Figure 15. SEM micrographs of representative KSL carbon material: (a) Prior to ball milling, particles are irregular with micro-scale sizes (10–40 μm), thus low surface area is exhibited; (b) After ball milling, a higher surface area is attained as particles improve in uniformity and sizes range in the nano-scale (64–178 nm).

Table 1. Characterization of surface as a function of reduction temperatures to KSL material according to BET analysis

Sample test [a]	**Total pore volume** ($mL\ g^{-1}$)	**BET surface area** ($m^2\ g^{-1}$)
After reduction (1050 °C)	0.046	78
After reduction (2000 °C)	0.067	74

[a] Outgas time was two hours with a temperature of 180 °C for all sample tests.

Table 2. Characterization of composition as a function of heat treatments to KSL according to elemental analysis

Sample test	**C (%)** [a] (± 0.2)	**H (%)** [a] (± 0.04)	**N (%)** [a] (± 0.03)
KSL	61.3	5.41	0.48
After pyrolysis (1000 °C)	79.5	0.51	0.75
After reduction (1050 °C)	88.3	0.05	0.90
After reduction (2000 °C)	95.2		0.26

[a] All composition values are expressed in weight percent (wt %) units.

The TGA results are summarized in Table 4 and Figure 16. These results were performed across the entire process from the raw KSL material to pyrolysis and reduced materials. The char content represents the last drop of the curve and resulted in roughly 42% for the starting KSL material. Char yields of over 88% and increasing after each heating step reveals that carbon content also increases as supported by previous elemental composition analyses. The increased char content indicates that each heat treatment removes some of the inorganic compounds and water. The averaged ash content for KSL material is 2.05%. Based on the thermal decomposition, the molecular bonds become stronger after each heat treatment. Structure of material becomes more rigid and the thermal decomposition increases after pyrolysis and even further after reduction reaching a decomposition temperature twice as high as the non-processed KSL.

Characterization of atomic structure

In order to better understand the extent of crystallinity due to graphitization imposed by the pyrolysis and reduction steps, the structure KSL materials were characterized by XRD. Figure 17 compares XRD patterns of KSL at various processing stages and a graphite powder standard as a means to provide insight of processing-structure relationships. Initially, KSL powder has a smooth and broad pattern with few distinguishable peak reflections. With a peak positioned at 21.09° and ordered domain size of 0.74 nm which is in agreement with reported results of KSL showing a peak positioned at 19.42° with an ordered domain size of 0.67 nm [61]. KSL is an amorphous polymer that exhibits colloidal structure with a dispersed higher molecular weight phase contributing to the amorphous halo. These peaks are affected by the relative distances and spaces between parallel and edge on aromatic rings. Sulfate groups contamination in the KSL structure can assist in forming graphitic structure [62, 63]. The presence of (002), (100), (101), and (110) reflections after pyrolysis at 1000 °C indicates the formation of crystalline domains in the material. Sharper and increasingly well-defined peaks after reduction indicate graphite crystallites formation as verified by comparison with graphite powder standard. Further graphitization is observed as reduction temperature increases. Analysis of (002) reflection reveals a crystallite size of0.84 and

Table 3. Characterization of composition as a function of heat treatments to KSL according to ICP analysis

Sample test	Na (%) [a] (± 0.01)	S (%) [a] (± 0.01)	Fe (%) [a] (± 0.02)
KSL	1.00	1.61	0.00
After pyrolysis (1000 °C)	1.72	1.23	0.43
After reduction (1050 °C)	2.19	1.41	5.40
After reduction (2000 °C)	0.02	0.22	0.15

[a] All composition values are expressed in weight percent (wt%) units.

Table 4. Thermal decomposition and char content as a function of heat treatments to KSL according to thermogravimetric analysis

Sample test	Sample mass (mg)	Thermal decomposition (°C)	Char content (%) [a]
KSL	7.93	304	41.95
After pyrolysis (1000 °C)	8.70	596	88.38
After reduction (1050 °C)	9.52	652	91.35

[a] Char content values are expressed in weight percent (wt%) units.

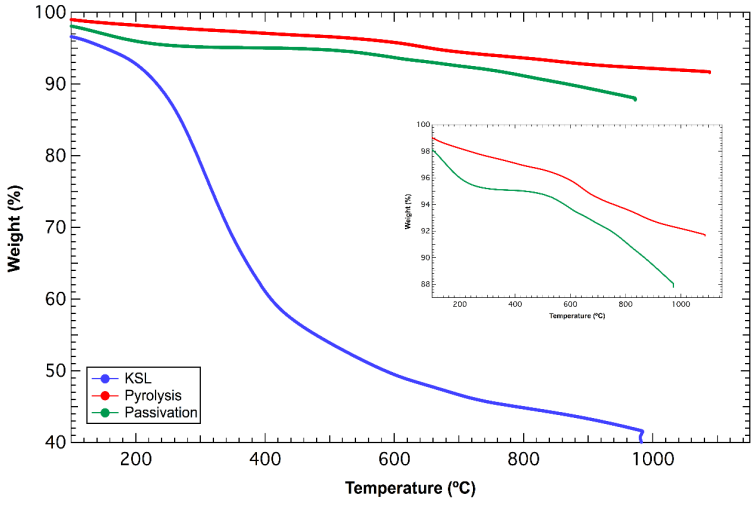

Figure 16. Thermal decomposition of KSL materials under nitrogen atmosphere at 10 °C min^{-1}. The initial KSL material went through pyrolysis step at 1000 °C and reduction step at 1050 °C. The weight percent of the char content increases after heat treatments from 40 to 90% due to larger remains of carbon content. The inset highlights the thermal decomposition of the pyrolyzed (596 °C) and reduced (652 °C) materials when averaged over multiple samples.

1.73 nm for reduction temperatures of 1050 and 2000 °C, respectively. XRD peaks of KSL exhibit broadening because the crystallite sizes are small compared to graphite that has sizes of 19.53 nm for (002) and 14.69 nm for (100) reflections. The interatomic spacing shown in Table 5 agrees with an evolution in graphite domains at high temperature processing. In crystallography, symmetry operations of molecular arrangements are described by rotation and translation transformations. Graphite has a stable structure and the changes of d-spacing for plane (002) may be attributed to translation of graphitic sheets [34]. Furthermore, crystal planes of the form (hkl) are influenced by translational stacking faults, this behavior can be observed in the 2000 °C sample by the appearance of the (101) plane [47]. It is important to note that graphite formation is characterized by the (101) reflection [61]. We assume the (112) peak is characteristic of the KSL material since it disappears after processing. Previous study reveals that basal and edge surface planes of graphite play an important role during lithium intercalation [64]. During battery operation, lithium-ions mainly intercalate with the graphite electrode through edge planes, thus producing different SEI formations between basal and edge sites. The basal-to-edge-plane ratio helps characterize electrochemical performance. Our nanographitic material contains more surface area in the edge planes compared to basal planes, thus enhancing lithium intercalation as well as electrochemical performance. A well-defined arrangement of graphitic layers, i.e. ABAB, is achieved from our processing material for electrochemical applications. As a result, this allows intercalation of lithium ions, which is essential for efficient functionality of batteries and prolongs life cycle.

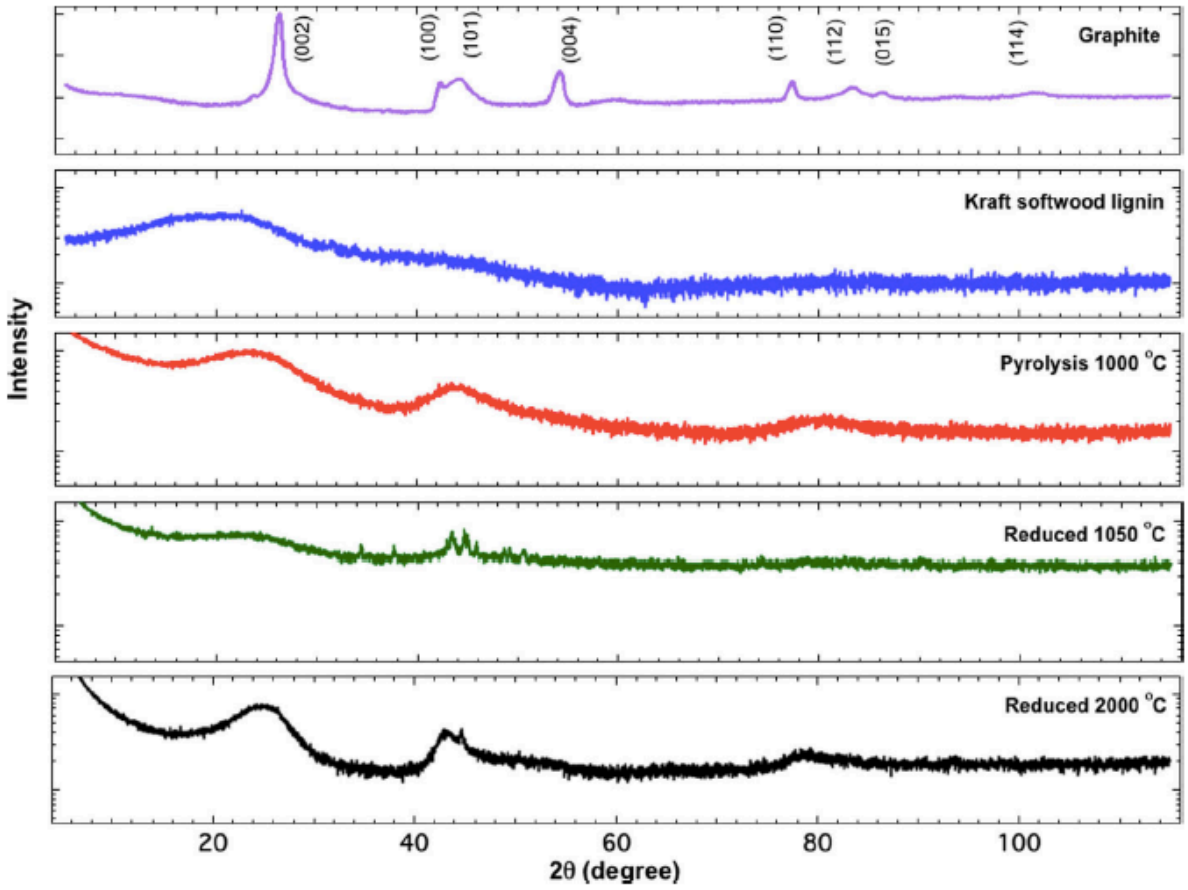

Figure 17. XRD patterns of non-processed and processed KSL. An indexed pattern corresponding to graphite powder is included for comparing structure graphitization. Heat treatments demonstrate the formation of graphitic domains as shown by the appearance of sharper peaks and the (101) reflection.

Table 5. Interatomic spacing of crystal planes as a function of heat treatments to KSL according to XRD analysis

Sample test	(002) [a]	(100) [a]	(101) [a]	(110) [a]	(112) [a]
After pyrolysis (1000 °C)	0.375	0.209		0.121	0.114
After reduction (1050 °C)	0.391	0.207		0.119	
After reduction (2000 °C)	0.364	0.210	0.203	0.120	

[a] All interatomic spacing values are expressed in nm units.

Structure-electrochemical property relationships

Electrochemical analysis can evaluate the potential use of lignin powders for energy storage applications. To quantify the effects of lignin powder processing on lithium-ion battery performance, half-cells containing KSL-carbon anodes and lithium-metal cathodes were investigated. The electrochemical experiments were conducted for 6 samples (each with three replicas) of lithium-carbon [56] half-cells each having specific processing conditions such as reduction temperature, cast size, C-65 carbon black additive, ball milling and potential range. Each half-cell is identified using a unique sample identifier and their processing conditions are tabulated in Table 6. Galvanostatic cycling against Li/Li+ was performed to determine rate performance for given ranges of upper cutoff voltage. Sample LiC-A shown in Figure 18a demonstrated 340 mAh g^{-1} average charge capacity in first 45 cycles with a sustained Coulombic efficiency of 96%, while LiC-B (Figure 18b) had poorer average capacity of 184 mAh g^{-1}, but an improved retention of 97%. LiC-A and LiC-B were cycled in respective potential regimes of 0.005–2 V and 0.005–1.2 V. Several observations were drawn from these initial tests. First, some degradation of the anode appears to occur when the battery is cycled up to 2 V, resulting in a low ion capacity. Therefore, subsequent testing was done with an upper cutoff voltage of 1.5 V. Second, the carbon anodes that had not been ball-milled did not provide a uniform coating, resulting in poor performance in some samples (not shown). Consequently, subsequent cells included carbon composite anodes that had been ball-milled. Third, the inclusion of carbon black additive was deemed beneficial to electrode conductivity and was retained in subsequent tests.

For the next two conditions, half-cells designated LiC-C and LiC-D were galvanostatically cycled across a range of current draws to ascertain rate performance (Figure 19a). The batteries with 3 mil coating were more stable than those with 2 mil coating over long term at high current rate demands, but 2 mil cells exhibited higher capacity at lower current draws. For long cycling and reduction at 1050 °C, the 2 mil anodes averaged 444 mAh g^{-1} during charging stage while 3 mil anodes sustained 315 mAh g^{-1}. Moreover, LiC-D experienced higher stabilization as the capacity recovered when cycled at 30 mA g^{-1} at the end and LiC-C seems to degrade at high current densities.

Table 6. Distinctive experimental properties for samples of lithium-carbon half-cells

Sample ID	Reduction temperature (°C)	Cast size (mil) [a]	C-65	Ball-milled	Voltage range (V)
LiC-A	1050	1	yes	no	0.005–2
LiC-B	1050	1	no	no	0.005–1.2
LiC-C	1050	2	yes	yes	0.005–1.5
LiC-D	1050	3	yes	yes	0.005–1.5
LiC-E	2000	2	yes	yes	0.005–1.5
LiC-F	2000	3	yes	yes	0.005–1.5

[a] The unit mil is a typical manufacturing dimension, 1 mil = 25.4 μm.

The higher specific capacity in the 2 mil samples indicates the capacity is limited by electrode conductivity where the conductivity is lower for the thick 3 mil coating. Part of the material didn't involve in the lithium intercalation. The capacity fade in the 2 mil samples could be due to poor cohesion between the lignin and carbon black and/or adhesion between the electrode and current collector.

One possible reason for the higher capacity retention in the 3 mil samples is that when some lignin material became inactive due to poor cohesion, the lignin material which did not participate in the charge/discharge previously was available and could contribute to the electrode capacity. Thus, the capacity fade is much slower. The capacity drop in the first cycle discharge capacity is due to the solid electrolyte interface (SEI) formation. Figure 19b overlays both the charge and discharge rates for the LiC-D sample. The battery performance remained consistent for both stages, providing support that the 3 mil KSL anodes are robust. For the final two tests, performance was evaluated for samples reduced at 2000 °C, LiC-E and LiC-F. In Figure 20, both charge and discharge capacities are shown for a current density of 7.5 mA g^{-1}. The 1050 °C samples (LiC-C and LiC-D) attained higher capacities than their 2000 °C counterparts (LiC-E and LiC-F). This demonstrates that reduction temperature plays a key role in the final capacity of such materials. From the 1050 °C samples, LiC-C achieved the highest capacity with more than 200 mAh g^{-1} for all cycles when compared to LiC-D.

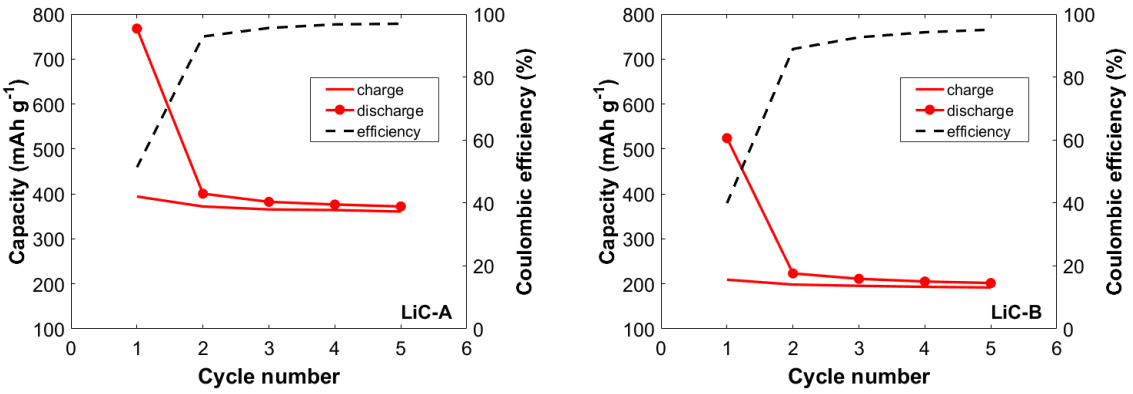

(**a**) (**b**)

Figure 18. Battery rate performance for non-ball-milled KSL anode reduced at 1050 °C and cycled at distinct potential ranges: (a) LiC-A voltage range was 0.005–2 V; (b) LiC-B voltage range was 0.005–1.2 V. In both samples, Coulombic efficiency monotonically increases during initial cycles.

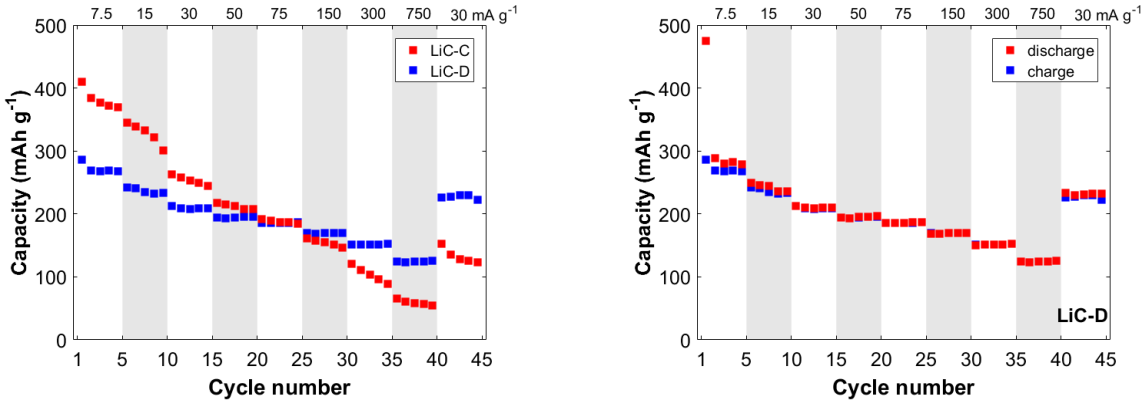

(a) (b)

Figure 19. Battery rate performance for ball-milled KSL anode reduced at 1050 °C and cycled at incremental current rates: (a) Charge capacity characterization for LiC-C and LiC-D; (b) Capacity characterization for LiC-D.

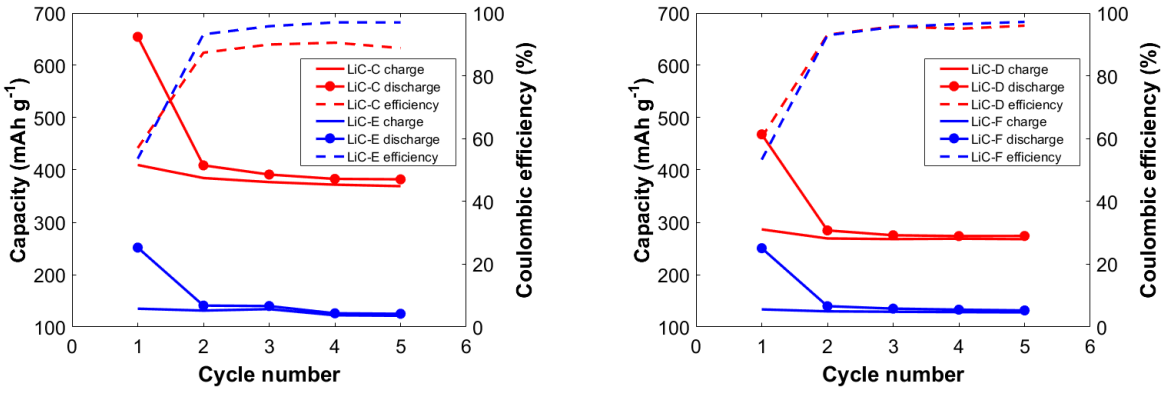

Figure 20. Battery rate performance of (a) 2 mil (LiC-C and LiC-E) and (b) 3 mil (LiC-D and LiC-F) coated anodes at 1050 and 2000 °C for current densities of 7.5 mA g^{-1} through 750 mA g^{-1}. Coulombic efficiencies over 90% are presented for both mil sizes and both reduction temperatures.

In a similar manner, LiC-E experienced approximately 100 mAh g^{-1} greater capacities than LiC-F. The smaller particle size and higher surface area of films reduced at 1050 °C, per Table 1, may facilitate the flux of lithium ions across the interface between the electrode and electrolyte, due to the suitable contact area [65]. We note that the anodes reduced at 1050 °C contain higher levels of contaminants (N, Na, S and Fe), per Table 2 and 3, but their presence does not diminish the capacity of these anodes. The effect of film thickness is also investigated in these samples. For both reduction temperatures, the batteries with 2 mil films exhibited higher capacity than those with 3 mil films. The cells with 2 mil films performed better than those with 1 mil films (LiC-A and LiC-B), though other conditions were also varied. The steady behavior of capacity and efficiency curves in Figure 20, support our proposed KSL processing in order to increase electrochemical reactions in carbon anode applications. Potential and capacity relationships due to galvanostatic cycling for samples LiC-C through LiC-F are shown in Figure 21, specifically for the first and third cycles. During the initial discharge cycle, all samples exhibit capacitance fluctuations that are degradations attributed to the SEI effect. For example, the LiC-C decays in capacity from 667 mAh g^{-1} to 405 mAh g^{-1} after voltage drops and ramps up again to 1.5 V. LiC-E and LiC-F appear with smoother capacity curves implying a microstructure less obstructive for ionic intercalations in

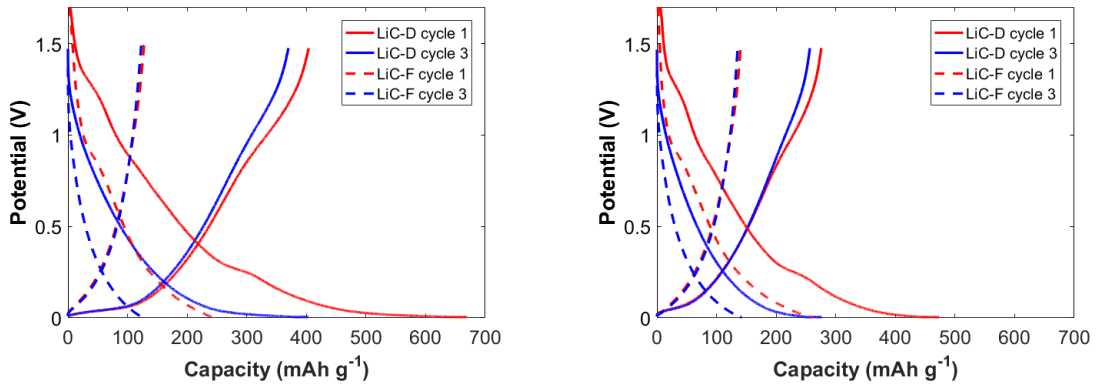

(**a**) (**b**)

Figure 21. Potential measurements per capacity rate for (a) 2 mil and (b) 3 mil samples during their 1st and 3rd cycles. Curves increasing in voltage correspond to charging cycles while decreasing ones are discharge cycles.

graphitic layers. The KSL carbon anodes demonstrate an improved specific charge capacity over organosolv lignin carbon fiber electrodes [47]. As a result, 2 and 3 mil samples have over 98% capacity retention after cycling. These results indicate KSL carbon anodes based on specific processing conditions are suitable for energy storage applications.

CONCLUSIONS

In this work, we have investigated kraft softwood lignin as a low-cost raw material for nanostructured carbon composites, with a variety of potential applications, including use as anodes in lithium-ion batteries. The processing required to convert KSL into a valuable product involves a set of carbonization steps including pyrolysis and reduction. During the carbonization process, a carbon composite develops which contains both crystalline (graphitic) domains and amorphous carbon domains. The reduction temperature can be used to control the size of the graphitic domains in KSL materials. Ball milling between the pyrolysis and reduction steps reduces the nominal particle size from 25 µm to nominally below 120 nm and results in a more homogenous material that can be incorporated easily into a battery.

Coin cells containing these resulting carbon composite anodes exhibited specific capacities per cycle in ranges of 180–250 and 300–450 mAh g^{-1} based mainly on

coating thickness and reduction temperature of active material. The latter capacities are comparable with performance of lithium-ion graphite that yields 372 mAh g^{-1}. Other factors that affect electrochemical performance such as the use of carbon black additive and potential ranges were also considered. Coulombic efficiencies of over 98% were sustained for extended galvanostatic cycles. The coin cell performance depended upon the set of processing conditions used to synthesize the carbon composite. The specific capacity of the carbon composite anode was 340 mAh g^{-1} for non-ball-milled samples of 1 mil and reduced at 1050 °C. For ball-milled samples of 2 mil, the specific capacity of the carbon composite anode increased from 165 to 444 mAh g^{-1} when the reduction temperature was reduced from 2000 °C to 1050 °C. The ball-milled samples of 3 mil experienced a capacity increase from 165 to 315 mAh g^{-1}. Consequently, a properly designed carbonization process for lignin is well suited to generating low-cost, high-efficiency electrodes.

ACKNOWLEDGEMENTS

Center for Renewable Carbon in the University of Tennessee, Knoxville, Institute of Agriculture, supported this work. This research at Oak Ridge National Laboratory, managed by UT Battelle, LLC, for the U.S. Department of Energy (DOE) under contract DE-AC05-00OR22725, sponsored by the Office of Energy Efficiency and Renewable Energy (EERE) Vehicle Technologies Office (VTO) Applied Battery Research Program (Program Manager: Peter Faguy). The authors would like to thank Ms. Choo Hamilton and Drs. Gabriel Veith, Omid Hosseinaei, Nicole Labbé and Nourredine Abdoulmoumine for research support.

CHAPTER 3

STRUCTURE AND DEFECTS IN GREEN AND CARBONIZED LIGNIN FIBERS USING RAMAN SCATTERING AND SANS

"This is the draft version of the following article: Garcia-Negron, V., Hosseinaei, O., Rios, O., Keffer, D., Pingali, S. V., Rials, T., Harper, D. P., Chmely, S. C. (2017), Structure and defects in green and carbonized lignin fibers using Raman spectroscopy and SANS, which is in process of publication.

ABSTRACT

The understanding of lignin structure is necessary for the development of processing-structure-property relationships for carbon composites in biofuel and energy storage applications. Yellow poplar hardwood and switchgrass were extracted using an organosolv process to obtain high purity lignin. Subsequently, these lignins and blends of these lignins were melt spun to produce green fibers. The purpose of the characterization of these fibers is to link the structural and physicochemical properties of green lignin fibers to the resulting carbon structure in carbonized lignin fibers. Small angle neutron scattering experiments were used to investigate the pore network as a means to link mechanical properties, structural surface, and orientation of lignin polymers in extruded fibers. These experiments were performed using solvents to maximize contrast. The lignin fibers were also carbonized and Raman spectroscopy was used to describe the degree and order of graphitization. Results show that green switchgrass lignin fiber contains a rougher surface structure compared to yellow poplar. The pores in green switchgrass are smaller than those in yellow poplar. However, the mechanical strength correlates almost exclusively to phenolic content from ^{13}C-NMR data. Raman experiments confirm that carbonized switchgrass fibers have a more ordered graphitic structure compared to yellow poplar. Structure and mechanical properties reveal significant defects in switchgrass fibers compared to yellow poplar and blended materials, most likely as result of the extraction and processing.

INTRODUCTION

The increase in demand of renewable carbon sources to produce carbon fibers is due to their value in a wide range of applications, mainly for fuel economy and energy savings. Efforts in agriculture areas from agencies, such as DOE and USDA, are committed to expand the production of biomass as a low-cost energy source and to replace petroleum consumption [66]. Lignocellulosic biomass is a potential renewable

source of biofuels and chemicals. Lignin is an aromatic polymer that is a byproduct of paper and biofuel production. It serves as an attractive precursor for carbon fiber technology. The development of lignin as an alternative fiber precursor to polyacrylonitrile (PAN) continues to be of interest to reduce fiber cost for applications that directly involve energy technologies: vehicles, aerospace, batteries, composite material, carbon fibers, and others.

One of the key challenges during production of these materials is to understand the development of carbon structure to improve fiber properties. These include understanding linkages and dynamics of molecular aggregates to improve graphitization. Moreover, genuine interest in the production of lignin spurs efforts for producing carbon materials due to its high purity carbon content and high thermal stability [67]. Modifying lignin and synthesizing lignin-based polymers can be a challenging task due to the random and heterogeneous nature of lignin polymer chains. The lignin polymer contains a somewhat random distribution of methoxyl, phenolic and aldehyde groups [68]. Methoxyl groups are radical and highly reactive making them very susceptible to polymerization with other groups including themselves. The phenolic groups consist of phenyl and hydroxyl groups. The former has an aromatic and crystalline structure with low reactivity (stable), while the latter is a radical OH. During polymerization methoxyl and hydroxyl combine by oxidation to form aromatic rings [68]. Aldehydes, which are slightly polar and composed of a carbonyl center with alkyl side chains, help during polymerization [69]. Grass structures generally lack methoxyl components enabling significant branching. In comparison softwoods and hardwoods contain measurable amounts of methoxyl and less branching than grasses. However, hardwoods have the highest methoxyl content and consequently, a more defined/organized structure.

The ratios of lignin precursors: coniferyl (G), p-coumeryl (H), and sinapyl alcohols (S), can vary depending upon type of wood. Hardwoods contain mainly G and S, whereas softwoods contain G and less H, and grasses contain more H [41, 70, 71]. S:G ratios can be estimated using semiquantitative and quantitative analysis. Volume integrals, interunit linkages relative to total side chains and correlation of C_2-H_2 are used for semiquantitative analysis. Carbon-13 Nuclear Magnetic Resonance (^{13}C-NMR)

spectroscopy was conducted for quantitatively estimating S:G ratios [67], refer to Table 10. In Jin's studies, they characterized red oak and yellow poplar, two types of hardwoods with varying S, G, and H units, and provide information from the elemental analysis. The respective elemental content for red oak and yellow poplar are: 47.03 and 47.58 for C%, 5.94 and 5.87 for H%, 0.30 and 0.37 for N%, and 0.19 and 0.20 for S% [70]. These compositions can serve as guides to understand the development of structure and resulting properties.

Small angle neutron scattering (SANS) studies and molecular dynamics simulations on loblolly pine lignin (softwood) reveal invariant fractal patterns that gives rise to the power law exponent on the surface of material aggregates [72]. Analysis on scattering data mainly depends on structure sizes, biomass composition, and the relative contrast between scatterings of different structures [73]. In Cheng they studied different lignin in solutions to obtain the sizes of basal subunits and its shape. Results indicate that sizes are about 200 nm and vary with lignin type. They also identified a relationship between elongated shapes of subunits and from the lignin solutions [74]. Carbon porosity is an important characteristic for many industrial applications such as adsorbents, graphitic foams, and anode batteries. Pore density is also a defect that can contribute to low mechanical properties in certain applications. SANS contrast matching has been used to decouple scattered data produced by both accessible and inaccessible pores, since all pores scatter neutrons in dry samples [75]. The technique involves filling the accessible pores in the surface with a liquid solvent that has the same neutron scattering potential as the solid material. As a result, only the scattered neutrons from inaccessible pores are detected, these can be compared with the total scattering to gain information about the accessible pores. The production of lignin fibers benefits from understanding how polymer additives improve the assembly of lignin aggregates from hardwoods, softwoods, and annual grasses. The addition of poly(ethylene oxide) to hardwood and softwood increased the length of a cylinder fit and hints at more extensively branched structure in softwoods [68]. These local and global structural alterations improve carbon fibers production since they limit defect formations.

Raman spectroscopy is used to understand the degree of graphitization of carbon materials. The non-destructive tool helps identify the D and G bands that are

characteristic of carbon materials and produced as result of vibrational frequencies. The G band is a first order peak associated with ordered structures composed of sp^2 C-C bonds. Disorder lengths and bond angles may also affect the G band [76]. On the other hand, the D band is attributed to defects in graphite lattices with sp^3 C-C bonds, which is indicative of edges and boundaries, that is, disordered structures [77]. The bands can be fitted using Lorenztian or Gaussian functions to obtain information such as full width half maxima (FWHM) and area under peak. Comparing relative peak intensities and areas, peak positions, and FWHM are common approaches to establish relationships of graphitization [37, 76, 77]. The FWHM is indicative of the purity of graphite structures represented by the peak, which increases as the peak becomes narrower. Tuinstra and Koenig relationship states that the ratio of intensities is proportional to crystallite sizes, L_α, [78]

$$\frac{I_D}{I_G} = \frac{C_\lambda}{L_\alpha}$$

where the constant, C_λ, depends on the laser beam excitation energy (in our case, C_λ ~4.96 nm). [78, 79]. In [80] the results of D and G peaks is 1360 and 1585 cm^{-1}, respectively, for the Raman shifts, meaning a significant disorder for their nanostructure carbon material as result of processing recycle tires. In another study graphitic carbon nanocage with hierarchical pore structure was synthesized showing high degree of crystallinity and graphitization [30].

Chapter 3 focuses on introducing structure properties of green lignin fiber and carbonaceous lignin product from the following two sources: switchgrass (*Panicum virgatum*), and hardwood yellow poplar (*Liriodendron tulipifera*), both extracted by organosolv fractionation. The main objective is to characterize lignin fibers from switchgrass, hardwood, and their blends, to understand how the choice of feedstock impacts the processing-property-structure relationship. The green lignin fibers were heat treated to carbon fibers via stabilization and carbonization methods. The fibers are evaluated at each processing stage to establish correlation between structure morphology and mechanical properties. SANS and Raman spectroscopy results are

used to visualize pore defects, surface shape, and crystallite aggregates, and to establish structural relationships of lignin due to controlled conversion processing.

METHODS

Lignin fibers preparation

The preparation of lignin fibers was conducted at Center for Renewable Carbon at The University of Tennessee-Knoxville, USA. Lignin from Alamo switchgrass (*Panicum virgatum*) and yellow poplar (*Liriodendron tulipifera*) was separated from whole biomass via organosolv fractionation following the method described by [10]. Table 7 provides a summary of the organosolv, extrusion and spinneret conditions. Melt spinning of the lignin was performed using a Haake MiniLab extruder (Thermo Scientific) with custom spinneret with a 200 μm orifice. Each type of lignin source is identified with unique sample identifier. The biomass extraction treatment consisted in a flow-through reactor with a mixture of methyl isobutyl ketone (MIBK), water, ethanol, and a concentration of sulfuric acid (H_2SO_4) to temperatures of 140 or 160 ºC [10, 81]. These factors were used to calculate a severity for each extraction conditions. The severity is a measure of how intense a treatment is in term of time, temperature, and acid concentration.

Lignin carbon fibers preparation

A selected set of blended lignin fibers was also characterized via heat treatments. The set of samples were stabilized with a Heratherm OGH60 (Thermo Scientific) convection oven and during carbonization a Lindberg-Blue M with a 25 mm tube furnace (Thermo Scientific) was used. More lignin fiber details can be addressed in [67]. Samples were stabilized under 250 $^{\circ}$C under air to the rate of 0.05°C min^{-1}. Followed by carbonization process consisted of two steps: (a) 600 $^{\circ}$C with 3 $^{\circ}$C min^{-1} and a 5 min hold at 600 $^{\circ}$C, and (b) 1000 $^{\circ}$C with 5 $^{\circ}$C min^{-1} and a 15 min hold 1000 $^{\circ}$C at 0.2 L min^{-1} in Nitrogen [67] The set of samples were used for Raman spectroscopy.

Table 7. Summary of processing conditions for green lignin fibers [67]

Sample ID	Type of lignin source	Organosolv extraction	Blended	Extruded & spinneret
SG_{LS}	Switchgrass	140°C, 0.05M H_2SO_4, 2hrs	-	180-185°C
SG_{HS}	Switchgrass	160°C, 0.05M H_2SO_4, 2hrs	-	190-195 °C
YP_{LS}	Yellow Poplar low severity	140°C, 0.05M H_2SO_4, 2hrs	-	180-185°C
YP_{HS}	Yellow Poplar high severity	160°C, 0.05M H_2SO_4, 2hrs	-	180-185 °C
$YP_{75}SG_{25}$[a]	75:25[a]	-	160 °C, 0.05M H_2SO_4, 2hrs	180-185 °C
$YP_{85}SG_{15}$[a]	85:15[a]	-	160 °C, 0.05M H_2SO_4, 2hrs	180-185 °C

[a] by w/w%- YP:SG

Table 8. Volume content of mixtures used as solvents in SANS experiments.

Sample mixture	Mixture of H & D Pentanes [a,b]	Ethyl Acetate [a]	D_2O	Dry
1	-	-	-	100
2	-	-	100	-
3	70	30	-	-

[a] by v/v%

[b] H-Pentane (46%) - D-Pentane (54%)

Small angle neutron scattering

Experiments were conducted using Bio-SANS (CG-3) instrument at the High Flux Isotope Reactor facilities located in Oak Ridge National Laboratory. Samples were mounted in a titanium cell provided on site, and cell configuration includes the following components: two quartz window, two ultra-chemical resistant Kalrez O-ring, and titanium spacer of 0.5 mm. The lignin fibers were mounted between the quartz windows, and then solvent was injected. The lignin fibers were mounted between the quartz windows, and then solvent was injected. The Q-range covered was ~0.0015–0.4 $Å^{-1}$, with two configurations, 6 Å and 12 Å neutrons. To understand pore structure a contrast matching technique was performed with various solvent mixtures that are shown in Table 8. SANS software packages in Igor Pro platform and SAS data analysis were used for data analysis.

Raman spectroscopy

A WiTec instrument was used to acquire Raman spectra with an Alpha 300 confocal Raman microscope. The excitation laser wavelength of 532 nm, a 20x objective and 600 grooves per millimeter grating were setup. The laser spot size was about 1 μm and data was collected from a minimum of 180 min. Spectral were normally collected from a range of 400 to 2600 cm^{-1} Raman shift. Lignin carbon fibers were mounted in epoxy, 2-dimethylaminoethanol (DMAE) hardener and nonenyl succininc anhydride (NSA) EM grade resin from Ted Pella, INC, and polished to analyze a single fiber cross-section.

RESULTS AND DISCUSSION

The green lignin fibers produced from switchgrass, yellow poplar, and related blends were characterized using ^{13}C-NMR and ^{31}P-NMR in [67]. These techniques served to identify differences between lignin structures in terms of aromatic and hydroxyl groups. ^{13}C-NMR experiments show that yellow poplar contains higher amounts of aromatic methine carbons compared to switchgrass high severity, 2.0 mmol g^{-1} and 1.65 mmol g^{-1}, respectively. On the other hand, yellow poplar (2.19 mmol g^{-1}) contains lower amounts of oxygenated aromatic carbons than switchgrass high severity

(2.44 mmol g^{-1}). The content of aromatic C-C structures in yellow poplar (1.81 mmol g^{-1}) is lower than in switchgrass high severity (2.31 mmol g^{-1}). Switchgrass has a higher presence of condensed aromatic structures and presumably has higher carbon yield. A similar trend occurs between yellow poplar and switchgrass of low severity. The tensile strength is extremely highly correlated (a correlation coefficient of 0.998) with phenolic content (refer to Table 10). Other weaker correlations between tensile strength and physical properties are results of correlations through the phenolic content.

Quantitative ^{31}P-NMR measurements of carboxylic acid OH, phenolic OH, and aliphatic OH groups are presented in Table 9. Carboxylic acid OH and p-hydroxyphenyl are lowest for both yellow poplar at high and low severities, whereas switchgrass samples have the highest. The C_5 substitutes predominate in the high severity samples and YP_{85} SG_{15}. On the other hand, switchgrass resulted with least content of phenolic OH (1.65 and 2.20 mmol g^{-1}), and YP_{HS} had the highest (3.70 mmol g^{-1}). The low severity fibers have the highest content of aliphatic OH. ^{31}P-NMR data shows a negative correlation (a correlation coefficient of -0.861) between aliphatic OH groups and tensile strength. A slight correlation of phenolic groups and tensile strength is noted with a correlation coefficient 0.642. The monomeric units in green lignin fibers vary and differ depending on lignin source, having an effect on lignin structure. From [67], pretreatment comparisons between switchgrass and yellow poplar show that higher severity increases phenolic-hydroxyl groups while decreases aliphatic-hydroxyl groups. The stability of aliphatic-hydroxyl units prevents complete fusion during spinning causing pores to form during fiber processing (stabilization and carbonization). Table 10 includes a summary of S:G ratio and tensile strength measured in previous work by [67]. These materials results show that yellow poplar at high severity has a higher tensile strength compared to switchgrass. However, the two blended samples produced fibers with the highest tensile strengths.

Table 9. Hydroxyl group contents of lignin samples obtained by quantitative ^{31}P NMR spectroscopy (mmol g^{-1}).

Sample ID	Carboxylic acid OH (COOH)	Phenolic OH				Total phenolic OH	Aliphatic OH
		p-hydroxyphenyl	C_5 substituted	Guaiacyl	Syringyl		
SG_{LS}	0.18	0.49	0.19	0.62	0.35	1.65	2.84
SG_{HS}	0.17	0.60	0.34	0.71	0.55	2.20	2.05
YP_{LS}	0.04	0.03	0.23	0.56	1.46	2.28	2.69
YP_{HS}	0.04	0.06	0.38	0.70	2.56	3.70	1.49
$YP_{75}SG_{25}$	0.08	0.07	0.20	0.62	1.91	2.80	1.90
$YP_{85}SG_{15}$	0.06	0.03	0.32	0.55	2.05	2.95	1.59

Table 10. Comparisons of yellow poplar (YP), switchgrass (SG) lignin, and blends.

Sample ID	S:G ratio	Tensile strength of C-fiber (MPa)
SG_{LS}	0.90	-
SG_{HS}	0.64	370
YP_{LS}	3.0	346
YP_{HS}	1.2	544
$YP_{75}SG_{25}$[a]	1.18	607
$YP_{85}SG_{15}$[a]	1.20	747

LS = low severity (1.91), HS = high severity (2.50), where severity refers to the organosolv fractionation conditions by which the lignin is isolated from whole biomass. S:G ratio is the ratio of syringyl- to guaiacyl-type monomers in lignin

Small angle neutron scattering

SANS allowed a deeper understanding of polymer morphology and structural arrangement in green lignin fibers. Preliminary SANS experiments were conducted using green lignin fibers with D_2O, refer to Figure 22 and Figure 23, and Table 11. The scattering data is fitted using a two level approach. In the figures, the steep curve (on the left side) has a power law in the range of 3 to 4 and provides information about the polymer's surface smoothness. The right side of the curve where the power law is about 1 is related to porosity. A unified fit is constructed using the aforementioned level fits to estimates: R_g, power law exponent, and Guinier.

At short distance (about 1 m of distance from detector and 6 Å of aperture diameter) isotropic scattering hints that smallest particles were globular in shape, and thus may be approximated as spherical particles. Most of these particles were mono-dispersed in size (at least with in the resolution of the detector). At intermediate and long distances (about 6.8 m of distance from detector and 6 Å of aperture diameter and 15.3 m of distance from detector; 12 Å of aperture diameter), most samples displayed an anisotropic scattering. This implies that the shape of aggregate particles is anisotropic and may be approximated as ellipsoidal particles.

The arrangement inside the lignin fibers as seen by neutrons during SANS experiments is shown in Figure 24. The blue rectangle depicts the fibril axis, the light orange spherical particles are the smallest size observed (~1 nm), and the dark orange ellipsoidal particles are the aggregate particles (~100 nm). These sizes were preliminary estimates and give an idea that aggregate particle size seems to be shorter along the fibril axis and more elongated in the fibril cross-sectional plane. As a consequence, further experiments were targeted to obtain more confident results.

Contrast variation was used to resolve pore structure and particle sizes in the green lignin fiber. The setup of this experiment consisted of three scattering tests using switchgrass and yellow poplar lignin fibers. Scattering data was reduced with the background and then fit with SAS analysis. Table 12 presents SAS analysis of the reduced data, which are shown in Figure 25 and Figure 26. The first test was performed in air where dry fibers were setup in the beam line. Air scatters at maximum contrast, thus allowing detection of the largest sized particles in the fiber.

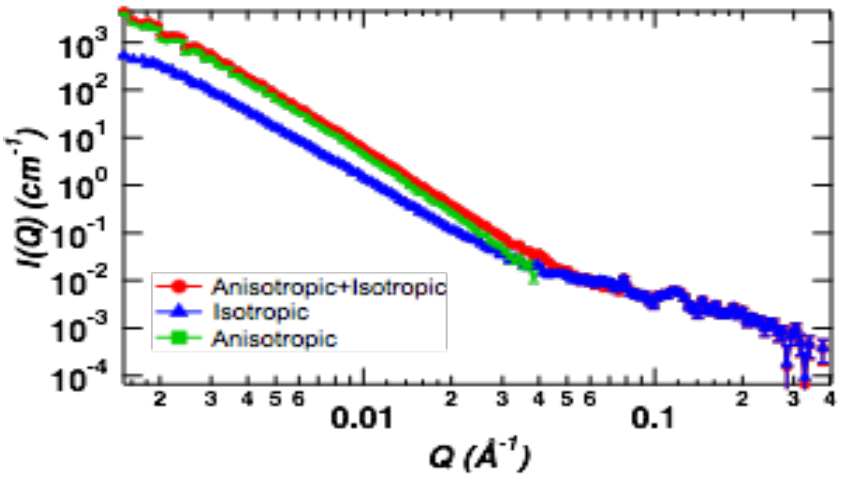

Figure 22. Example of scattering patterns for isotropic and anisotropic structures produced from green lignin fibers in D_2O.

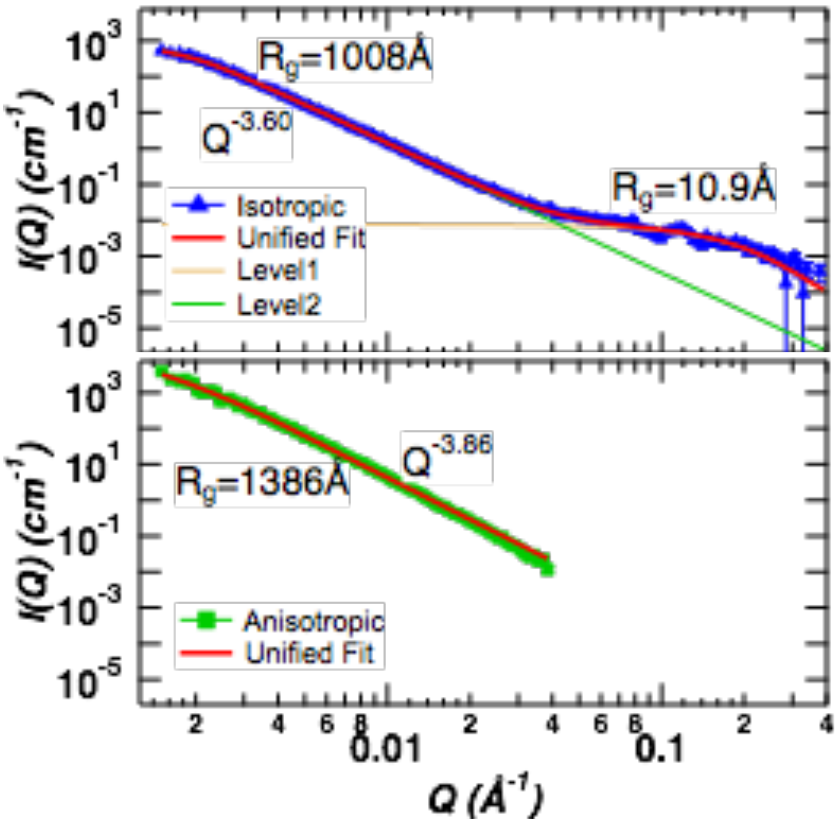

Figure 23. Example of scattering patterns for isotropic structures produced from green lignin fibers in D_2O. (top) The scattering data is fitted using two levels and a unified fit. The estimated radii of gyration resulted in 10.9 Å and 1008 Å. (bottom) The scattering data is fitted with a single unified fit, resulting with a radius of gyration of 1386 Å.

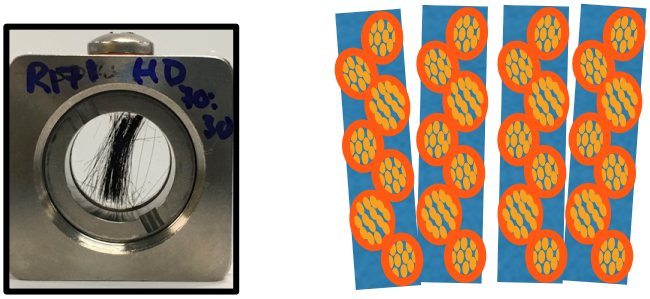

Figure 24. (left) Titanium sample holder with green lignin fibers suspended in solvent. (right) Arrangement of internal structure of lignin fibers as seen by SANS at varying distances. The small orange particles represent isotropic scattering regions with equal-sized particles, while the larger red particles correspond to aggregates at anisotropic scale.

The second test condition uses deuterium oxide since it does not wet nor destroy the fiber and allows air to sit in pores. Lastly, the third condition uses HD pentanes with ethyl acetate that likes to wet the fiber and penetrate the polymeric structure with the end result of pores being filled.

The unified fits in Figure 25 and Figure 26 show differences between pores and polymeric structure between switchgrass and yellow poplar. At low Q ranges, the small variations in scattering intensities may be attributed to the number of particles and we infer that they are similar. At high Q ranges, note that the D_2O curve has a hump, contrary to the other two conditions. This effect is interpreted as variations produced by the presence of pores. SAS analysis in high Q measured switchgrass and yellow poplar pores sizes to be ~10 Å and ~20 Å, respectively. Information on the number and volume of pores for YP and SG is included in Figure 27 and Figure 28. YP has fewer, larger pores compared to SG. Referring to Table 12, the radius of gyration is used to estimate the average size of particles and the Guinier value represents the smallest size of a particle observed. Since dispersity of particles is unknown, the assumption that there is a distribution of particle sizes is made. In the dry conditions, the Guinier size is actually larger than the particle average size indicative of either a poor fit or sample resolution. Nevertheless, particle sizes decrease as a solvent is added and the type of solvent wets more the fiber. The polymeric structure with the solvent mixture of HD pentanes and ethyl acetate resulted in a filled matrix including the inaccessible pores. The pore size

for HD pentanes mixture reveals an average particle size of about 650 Å for SG and 675 Å for YP, while the lower bound on particle size is ~100 for SG and ~95 for YP.

The power law exponent or Porod exponent indicates whether the surface fractal is rough or smooth. The power law of SG is in the range of 3 to 4 for the dry and D_2O conditions, this is characteristic of having rough surface fractals. YP_{HS} suggests having a smoother surface because it has a power law exponent of 4. The surface roughness is caused by aggregates or the individual particles. In summary SANS results reveal that switchgrass consists of a hyper branch polymeric structure, which is expected from the p-hydroxyphenyl monomeric unit and more G units. Moreover, the data shows smaller pores along a more packed structure compared to yellow poplar. The latter has bigger pores and a less packed structure.

Raman scattering

Raman scattering was performed to cross-sections of the lignin carbon fibers to get insights of graphitization degree, crystallite size, and purity of ordered and disordered structures [82]. Figure 29 presents images of the fiber cross-sections scanned during Raman procedure. Fiber diameters of sample cross-sections, Figure 29 and Table 13, were determined using ImageJ. The diameters varied from ~13 to 40 μm in size and do not seem to have significant impact in the analysis measurements. The collected and averaged spectra are shown in Figure 30. Spectra results from Table 13 identify two peaks, bands D and G, which are characteristic of graphitic materials [83, 84].

The Raman spectra of the lignin carbon fibers are compared with spectra from standard graphite powder in Figure 30. Graphite generates smooth Raman curves with a sharp G band located at 1585 cm^{-1}, which is three times greater in intensity than the D band at 1352 cm^{-1}. There are notable similarities and differences between LCF and graphite powder patterns. All LCF G peaks are broader and shifted to the right (near 1600 cm^{-1}); nevertheless, these peak magnitudes are comparable to that of graphite. The LCF D peaks, located closely to graphite's D shift, are even broader and have intensities comparable to their G counterparts. The shift of peaks is specific to the chemical bonds and symmetry of the molecules.

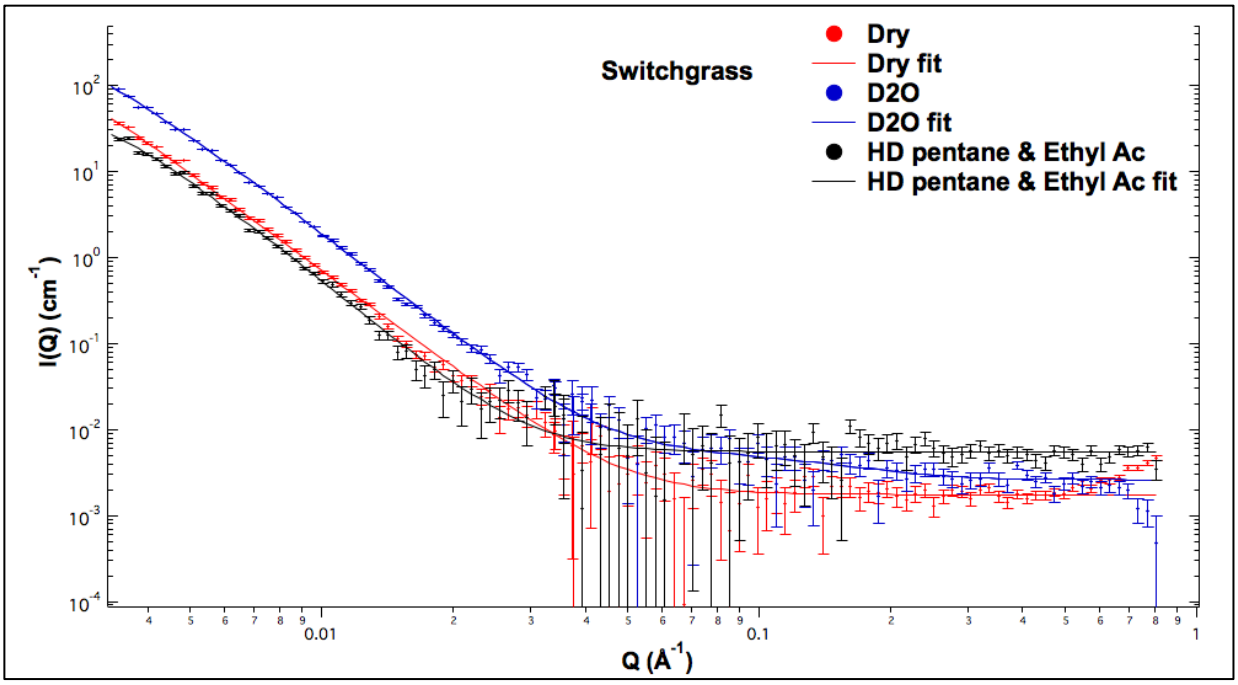

Figure 25. Scattering intensity of green lignin fibers in Q scattering vector for switchgrass in air, D_2O, and HD pentanes with ethyl acetate.

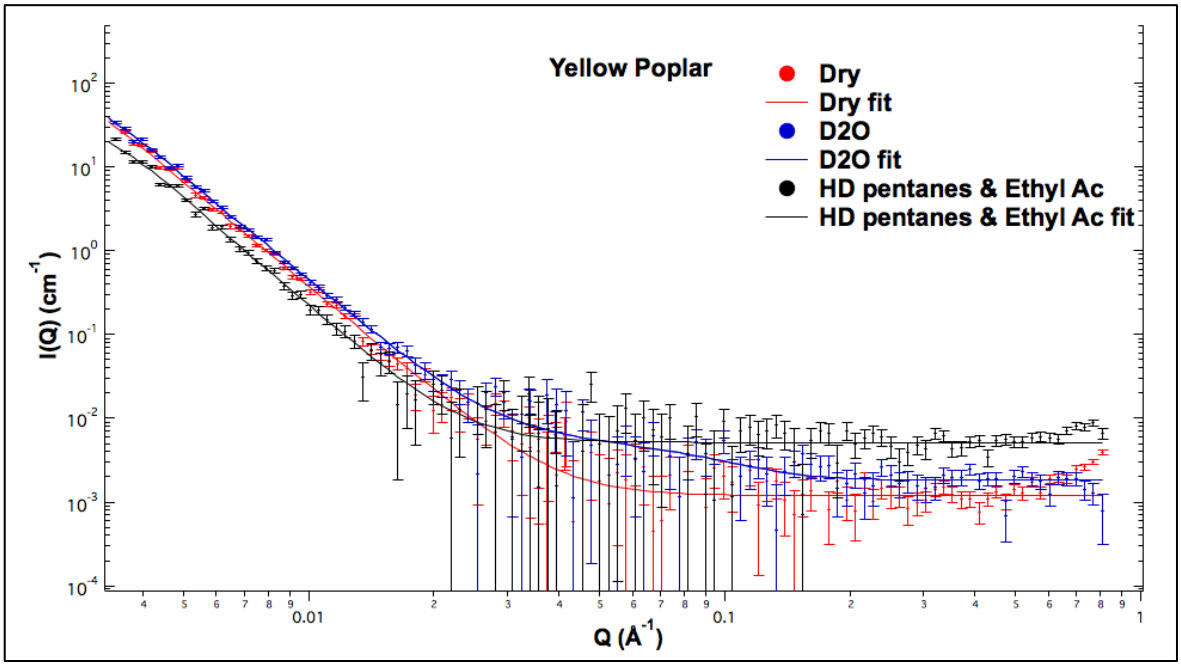

Figure 26. Scattering intensity of green lignin fibers in Q scattering vector for yellow poplar high severity in air, D_2O, and HD pentanes with ethyl acetate.

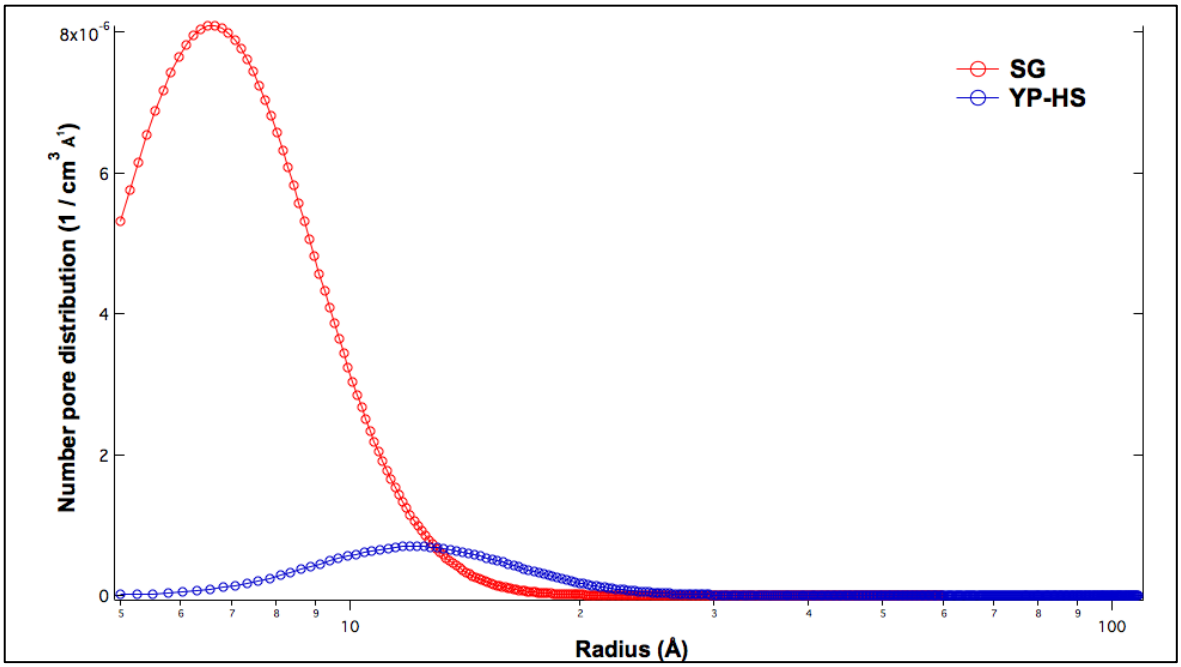

Figure 27. Number of pore distributions of green lignin fibers, switchgrass and yellow poplar, for D_2O condition.

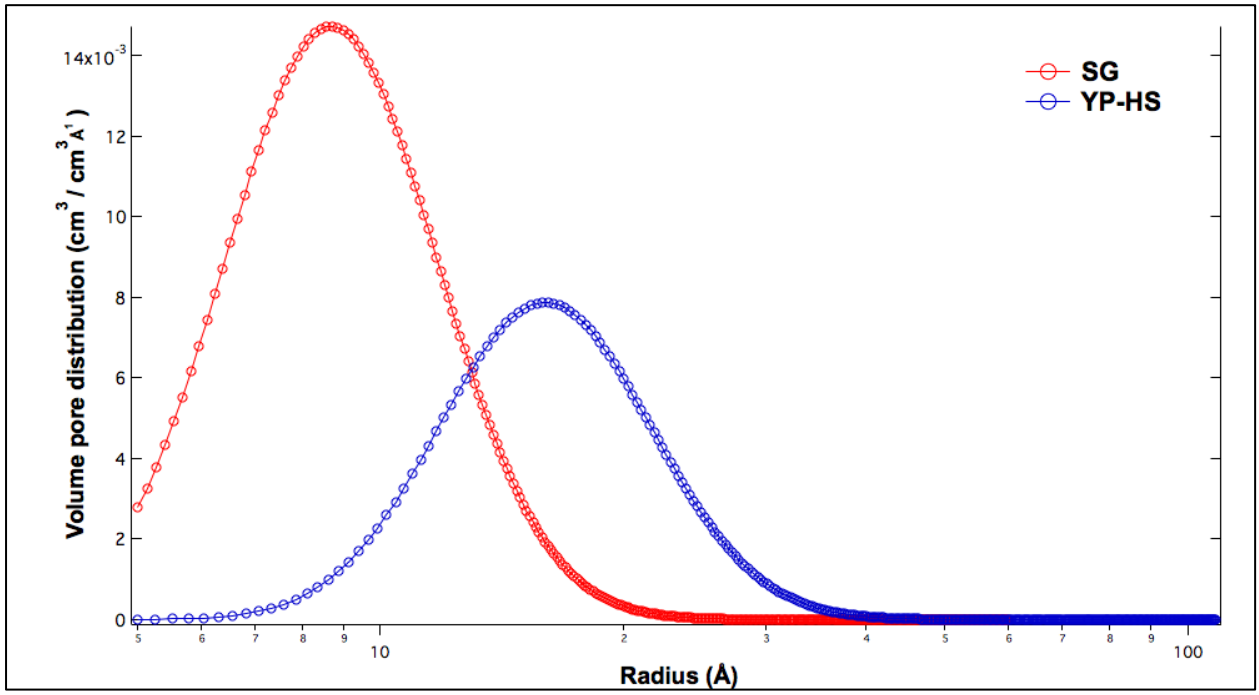

Figure 28. Volume pore distributions of green lignin fibers, switchgrass and yellow poplar, for D_2O condition.

Table 11. SANS analysis first batch of sample in D_2O.

Sample Name		Aggregates	Power-Law Exponent (–*P*)	Pores
		Radius of Gyration, R_g (Å)		Radius of Gyration, R_g (Å)
ISOTROPIC	SG	1007	3.6	11.7
	YP_{HS}	864	3.635	11
ANISOTROPIC	SG	1313	3.882	-
	YP_{HS}	1208	4.019	-

Table 12. SANS analysis second batch of sample.

Solvents	Sample Name	Aggregates	Power-Law Exponent (–*P*)	Guinier (Å)	Pores
		Radius of Gyration, R_g (Å)			Radius of Gyration, R_g (Å)
Dry	SG	1292	3.751	1467	-
	YP_{HS}	1368	4.145	1868	-
D_2O	SG	754.4	3.897	590.7	10.65
	YP_{HS}	744.1	4.145	243.2	19.6
HD pentanes:ethyl acetate	SG	648.9	4.118	111.6	-
	YP_{HS}	675	4.329	95.86	-

From the analysis in Table 13, switchgrass (SG) and blend ($YP_{85}SG_{15}$) attained the lowest and highest I(D)/I(G) ratios, respectively. This ratio is used as a density measure relating the abundance between disordered and ordered structures. Sample $YP_{75}SG_{25}$ estimates are similar to SG, while samples YP_{HS} and YP_{LS} are similar to $YP_{85}SG_{15}$. Graphite powder resulted with the largest crystallite size of 19.8 nm, followed by SG with 5.19 nm, and ending with blend $YP_{85}SG_{15}$ having the smallest size of 4.66 nm. This indicates a measurable presence of crystallinity within the fiber structure after carbonization. The crystallite sizes calculated with Raman scattering for graphite powder coincide with measurements obtained from XRD techniques; refer to Chapter 2 [41]. Furthermore, comparing particle sizes, pore structures, and crystallite sizes between the green fibers to the carbon fibers supports that morphological changes occur due to pyrolysis. For example, the crystallite sizes formed are an order of magnitude smaller than the average particle size from the green fibers. Keep in mind heat treatment foments depolymerization and the creation of polycyclic aromatic carbons.

Additional morphological and structural analyses make use of the integrated intensities and the FWHM; therefore, Raman spectra were fitted using Lorentzian curves. Table 14 summarizes the fitted data analysis and Figure 31-36 show the raw and fitted spectra for each LCF specimen. Band shifts, intensity ratios, and crystallite sizes remain similar to those from the raw spectra. The graphitic purity of structures increase as bands become well defined and thinner, that is, FWHM decrease. For the G band, all LCF's FWHM range between 90-95 cm^{-1} as compared to graphite powder with a FWHM of 32 cm^{-1}. The D band FWHMs show greater variance, 233–253 cm^{-1}, and are one order of magnitude greater than graphite, indicating traceable amounts of amorphous structures. Relative integrated intensities, A(D)/A(G), state that SG has the highest degree of graphitization due the lower ratio of areas, and $YP_{85}SG_{15}$ has the least degree of graphitization. A clear trend is that LCF made from switchgrass has the highest graphitic order.

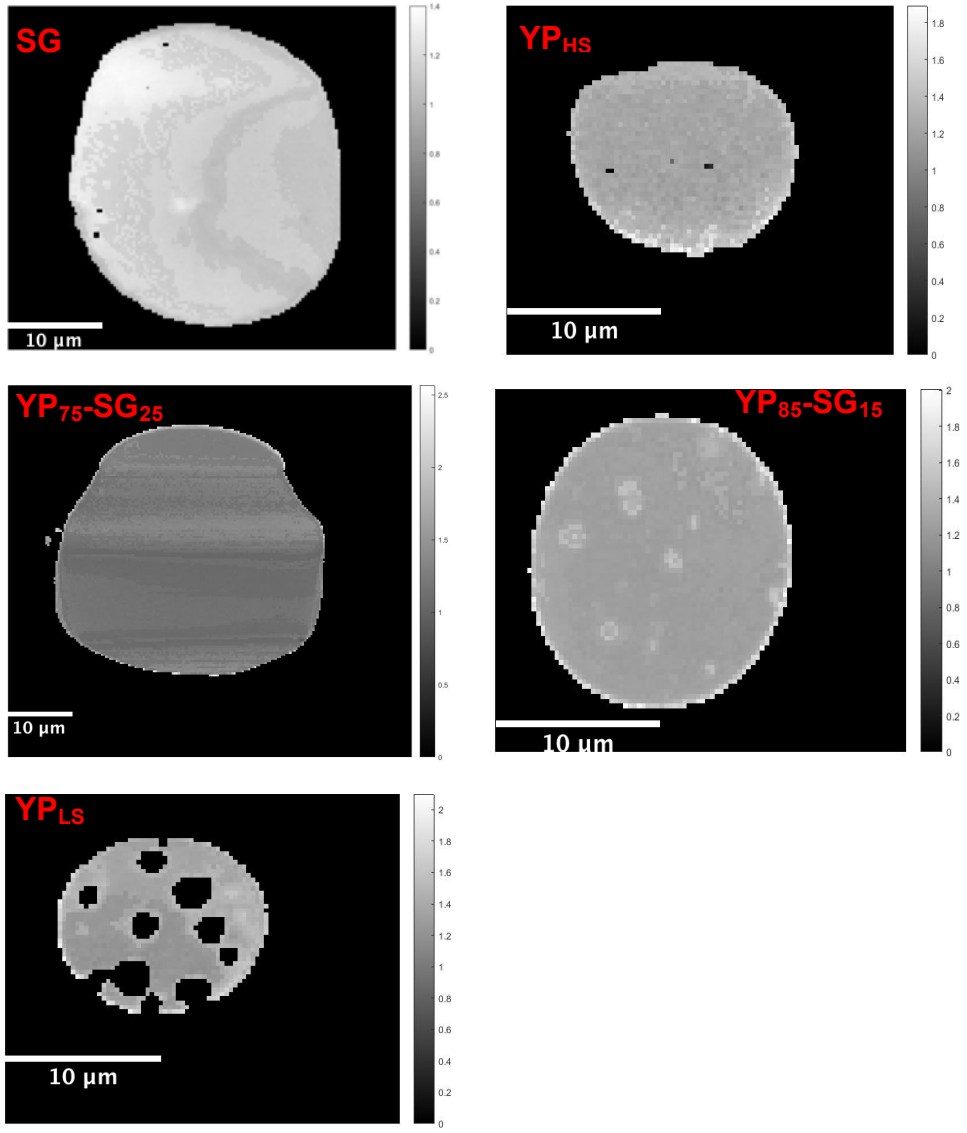

Figure 29. Cross-section images of switchgrass and yellow poplar lignin carbon fibers used for Raman spectroscopy experiment. The light colored regions represent the sample and the darker ones correspond to the epoxy background. The background was filtered prior to averaging spectra patterns.

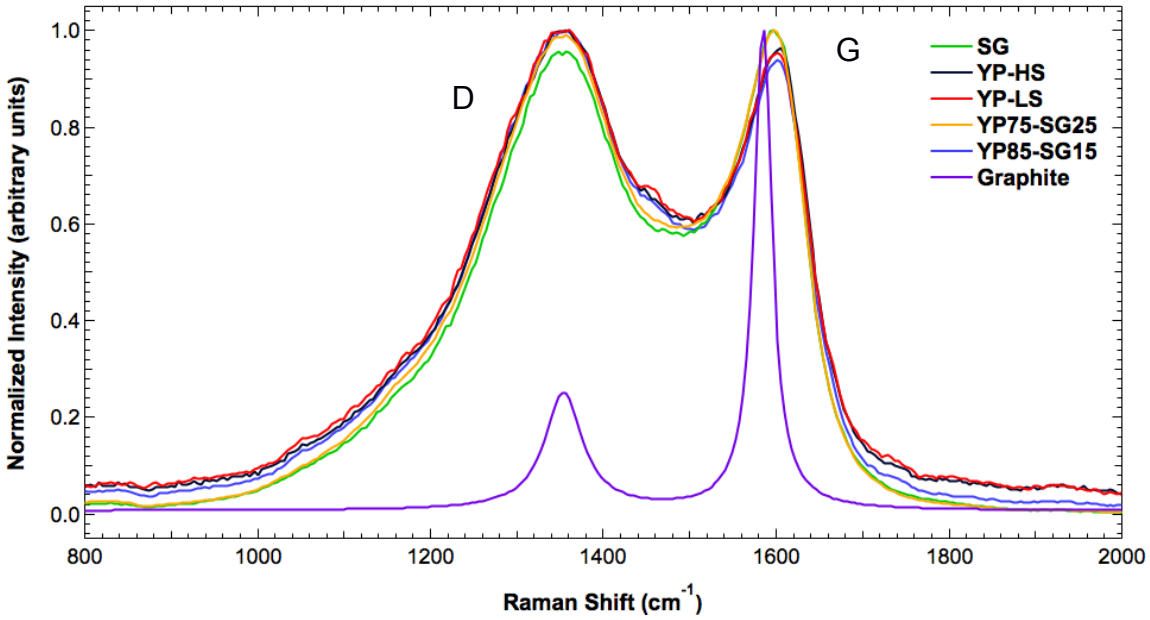

Figure 30. Average Raman spectroscopy of all lignin carbon fibers cross-section.

Table 13. Raman scattering analysis of lignin carbon fibers.

Sample name	**D-band Raman shift (cm^{-1}) (±1.6)**	**G-band Raman shift (cm^{-1}) (±3.0)**	**I_D/I_G ratios (±0.040)**	**Crystallite size (nm) (±0.194)**	**Fiber diameter (µm)**
SG	1356.6	1597.8	0.956	5.187	28.96
YP_{LS}	1356.6	1601.9	1.046	4.742	13.59
YP_{HS}	1352.5	1605.9	1.036	4.787	14.59
$YP_{75}SG_{25}$	1356.6	1597.8	0.990	5.009	39.59
$YP_{85}SG_{15}$	1356.6	1601.9	1.065	4.658	15.78
Graphite	1352.6	1585.9	0.251	19.754	-

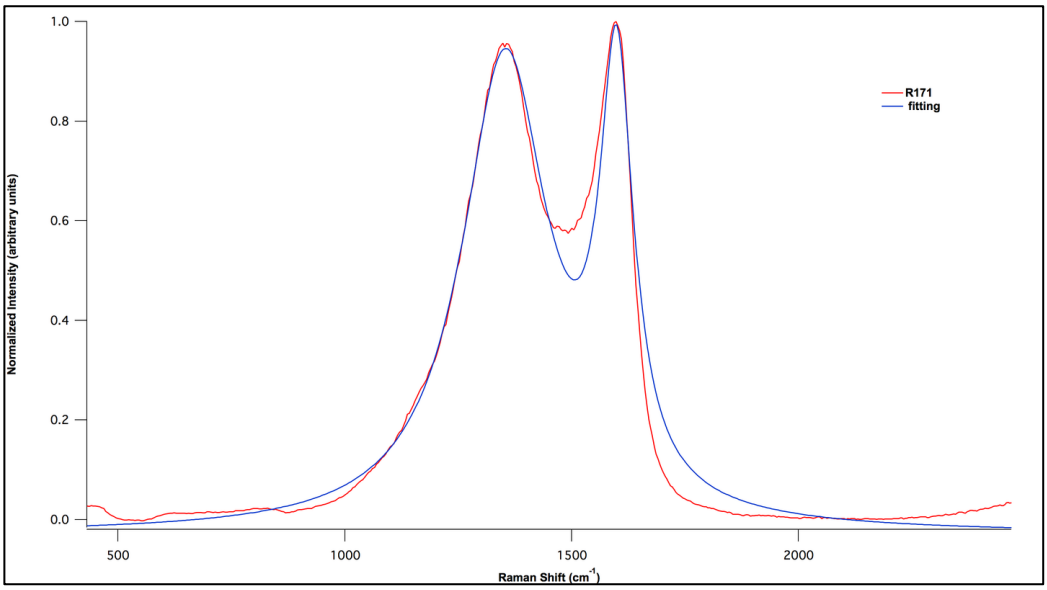

Figure 31. Raman spectroscopy and Lorentzian fit for cross-section lignin carbonized fiber switchgrass.

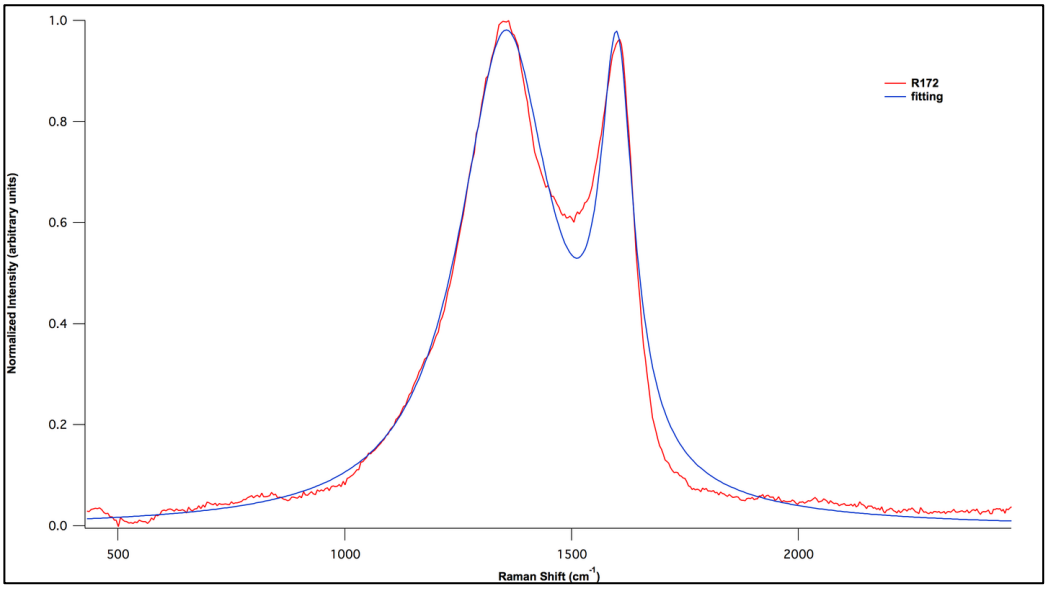

Figure 32. Raman spectroscopy and Lorentzian fit for cross-section lignin carbonized fiber yellow poplar high severity.

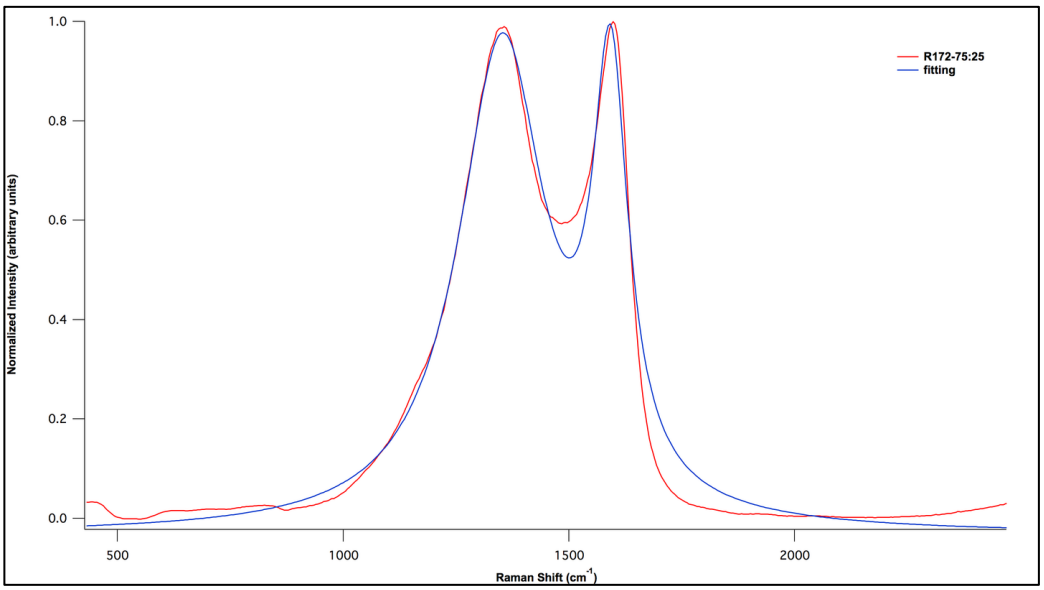

Figure 33. Raman spectroscopy and Lorentzian fit for cross-section lignin carbonized fiber yellow poplar 75 wt. % and Switchgrass 25 wt.%.

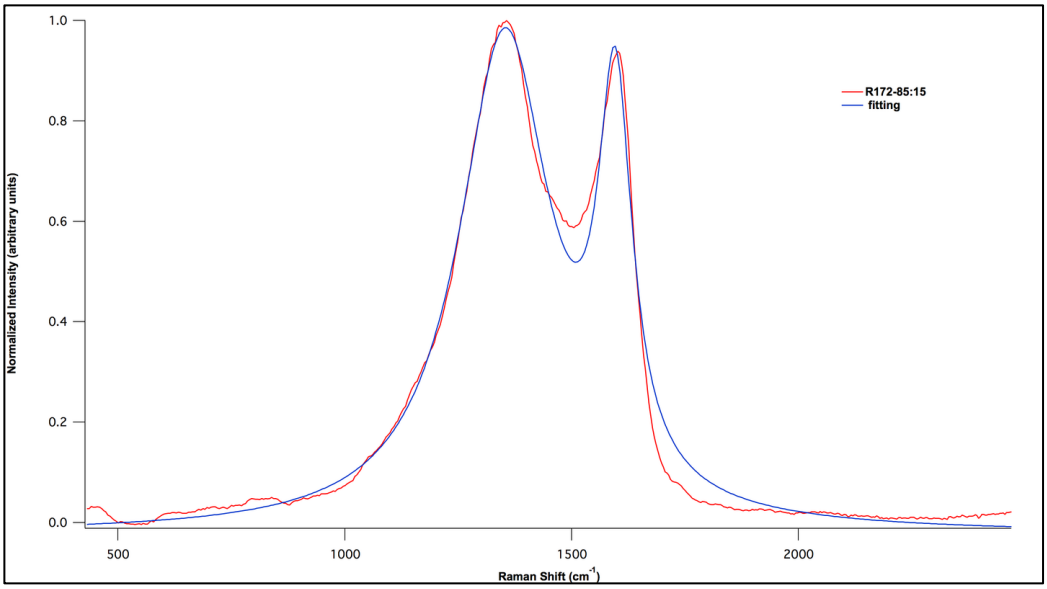

Figure 34. Raman spectroscopy and Lorentzian fit for cross-section lignin carbonized fiber yellow poplar 85 wt. % and switchgrass 15 wt.%.

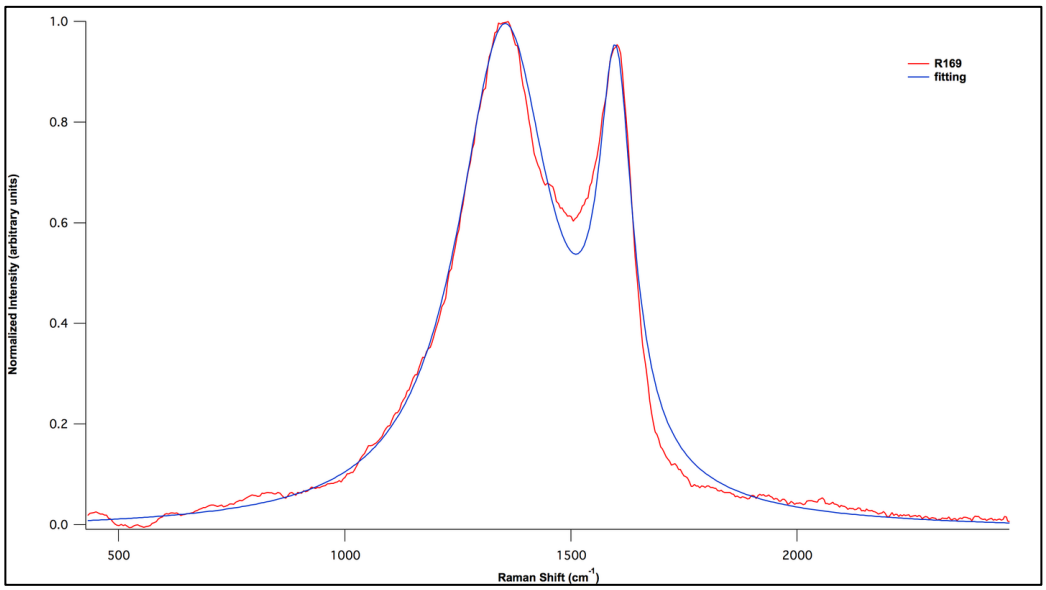

Figure 35. Raman spectroscopy and Lorentzian fit for cross-section lignin carbonized fiber yellow poplar lower severity.

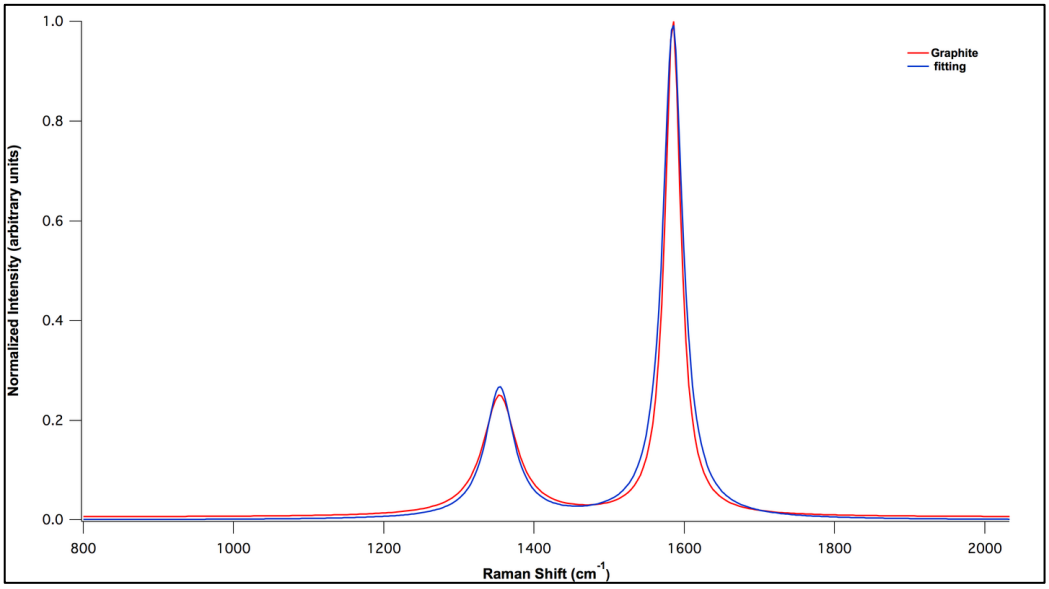

Figure 36. Raman spectroscopy and Lorentzian fit for graphite powder used as reference material.

Table 14. Raman scattering of fitted curves using Lorenztian analysis of lignin carbon fibers.

Sample name	D-band Raman shift (cm^{-1}) (±1.2)	G-band Raman shift (cm^{-1}) (±3.2)	I_D/I_G ratios (±0.033)	FWHM (D-band) (±8.1)	FWHM (G-band) (±2.1)	Crystallite size (nm) (±0.173)	A_D/A_G ratios (±0.285)
SG	1354.4	1599.5	0.952	233.3	90.0	5.210	2.891
YP_{LS}	1354.6	1594.4	1.045	253.0	93.0	4.747	3.507
YP_{HS}	1356	1599.7	1.002	250.3	90.0	4.950	3.399
$YP_{75}SG_{25}$	1353.4	1591.3	0.998	236.0	95.0	5.055	2.902
$YP_{85}SG_{15}$	1356.9	1596.1	1.039	247.4	90.0	4.775	3.511
Graphite	1354.9	1585.6	0.270	46.0	32.0	18.343	0.381

After showing a summary of the results of green lignin to carbon fibers comparison of these results proves that mechanical properties, such as tensile strength, have a lower tensile strength for switchgrass compared to yellow poplar and their blended fibers [67]. This is supported by SEM micrographs containing visible defects on the surface of these fibers, noting that yellow poplar has less defects than switchgrass [67]. The assumption is that the fiber processing causes defects. However, when we observe the nanomechanical properties of these materials switchgrass has a reduced modulus of 33 GPa and yellow poplar high severity 30.2 GPa. For the hardness of these materials switchgrass has a 5.69 GPa and yellow poplar high severity has 5.18 GPa [67]. Demonstrating that the monomeric structure of the switchgrass is suitable and promising for the carbon fiber applications.

CONCLUSIONS

Investigation of processing-structure-property relationship has been studied for two types of lignin sources extracted via organosolv fractionation, switchgrass and yellow poplar. These two sources were compared as green lignin fibers and carbonized fibers. Small angle neutron scattering was performed for the green lignin. Non-blended fibers and blends composed of both lignin types were studied for carbonized samples using Raman spectroscopy. The chemical modification of these fibers during blending and the varied processing severity impacts their mechanical properties. Contrast

variation was used to resolve pore structure and particle sizes using different solvents. Switchgrass has smaller but higher presence of pores than yellow poplar. Also, yellow poplar fibers attained a smoother surface compared to switchgrass fibers. The small pores in switchgrass lignin might occur as a result of its highly branch structure within the matrix. Furthermore, switchgrass produced larger crystallite sizes but demonstrated a lower tensile strength than yellow poplar. The product materials show evidence of a potential graphitic structure suitable for carbon fiber applications.

Characterization results demonstrate that green lignin fibers from switchgrass contain more G units than S units. Also, the structure of the carbonized switchgrass fibers had less disordered structures compared to all other fibers. This indicates there exists an inverse correlation between G units content and amount of disorder domains in the carbonized structure. ^{13}C-NMR study revealed a significant correlation among phenolic groups and tensile strength, while ^{31}P-NMR study identified a negative correlation between aliphatic groups and tensile strength. Additional relationships connecting feedstock structure to carbonized fiber structure may be explored. For example, compare volume fraction of crystalline domains and crystallite sizes of carbon composites. This study can be enhanced with XRD and BET experiments to compare crystallinity, porosity, and surface area measurements. Ultra-SANS and ultra-SAXS experiments (Q range < ~0.005 $Å^{-1}$) will help understand the internal hierarchical structure of polymeric units. Furthermore, incorporating softwood lignin fibers into the experiments will allow a more complete picture to establish processing-structure-property relationships of these materials.

ACKNOWLEDGEMENTS

The Center for Renewable Carbon at the University of Tennessee, Knoxville, Institute of Agriculture, supported this work. The authors would like to thank, Dr. Omid Hosseinaei for lignin fiber preparation, Dr. Jagjit Nanda and Dr. Rose Ruther for Raman experimental support. Access was granted through user proposal (1) S. Chmely, D. P. Harper, V. Garcia-Negron, T. Rials. Visualizing porous defects and lignin supramolecular structure in lignin fibers using complementary SAS techniques. ORNL HFIR Bio-SANS beam time. [IPTS-18060.1]; November 16, 2016. (2) S. Chmely, D. P.

Harper, T. Rials. Lignin intermolecular interactions that govern lignin fiber properties. ORNL HFIR Bio-SANS beam time. [IPTS-14356]; October 23-26, 2015. Thanks to the HFIR facility access and staff support during beam time at CG-3 station at Oak Ridge National Laboratory.

CHAPTER 4
CONCLUSIONS

CHAPTER CONCLUSIONS

Lignin is a natural amorphous polymer suitable as a graphite substitute for commercial carbon materials. Investigating lignin properties, extraction methods, and characterization techniques, combined with an understanding of the resulting carbon structure, helps associate the product material with synthetic carbon materials. Moreover, finding alternatives for kraft product applications, such as producing carbon materials, makes it attractive due to its lower cost ($0.04/kg lignin value as fuel in kraft pulp industries). Common lignin extraction methods and characterization techniques used in this study were presented. This is enhanced with a discussion of the general structure of carbon composites. Carbon materials have potential applications in the areas of electrochemical storage and automobile industries.

In Chapter 2, processing-structure-property relationships for different types of lignin sources were investigated by varying the processing temperature, time, and environment. The lignin sources considered are kraft softwood, organosolv switchgrass, and ogranosolv hardwood. Also, the processing-structure relationships of these materials to produce a carbon-based material were investigated using characterization techniques presented in Chapter 1. The study used the carbon material for developing lignin-carbon anodes in lithium-ion batteries. XRD analysis for heat-treated kraft lignin showed that while increasing temperature (e.g., 1050, 1500, and 2000 ºC) during carbonization, an ordered graphitic material was obtained. Particle sizes were controlled by ball milling techniques to attain homogeneity, and the presence of iron detected after ball milling is assumed to affect electrochemical performance. Similarly, it is likely that the presence of oxygen in the structure is the main reason for lower electrochemical performance. Under optimal processing conditions, a coin cell with a lignin-based anode demonstrated capacity superior to the theoretical maximum capacity of 372 mAh g^{-1} for graphite. Elemental analysis for lignin was presented during heat treatments, and as expected carbon content increased while the temperature increased. Results support that a properly designed carbonization process for lignin is well suited to generating low-cost, high-efficiency electrodes.

In Chapter 3, additional lignin sources were used to identify structure-properties-relationship. Comparisons between switchgrass, hardwood, and blends of lignin fibers

were made. Material structure was investigated by performing SANS experiments (of green fibers) coupled with Raman spectroscopy (after carbonization). Determination of the type of C-C bond was explored for cross-section surfaces of carbonized lignin fibers, and then compared to graphite powder peaks. The Raman spectra indicated a more ordered graphitic structure for switchgrass compared to blends and hardwood lignin. Moreover, these results support the presence of defects in the material during processing fibers. Characterization results demonstrate that green lignin fibers from switchgrass contain more G monomeric units than S units. This indicates that there exists an inverse correlation between G content and amount of disordered domains in the carbonized structure. A statistical analysis based on ^{13}C-NMR and ^{31}P-NMR data supports the presence of a positive correlation between phenolic groups and tensile strength. On the other hand, a negative correlation occurs between aliphatic groups and tensile strength.

SANS identified pores of larger sizes along the fibers in hardwood yellow poplar when compared to switchgrass. Also, SANS analysis dictates the presence of a less smooth surface in switchgrass than in yellow poplar. Pores in the nano scale are probably caused during fiber processing by the aliphatic groups that are volatile. Furthermore, switchgrass presents a lower tensile strength, 370 MPa, and lower tensile modulus, 34.7 GPa, as compared to the high severity yellow poplar with 544 MPa and 36.5 GPa, respectively. Hardwood yellow poplar processed under low severity conditions produced 346 MPa in tensile strength and 32.9 GPa in tensile modulus [67]. A set of preliminary experiments for SANS was used to have a first glance of the fiber structures and note flaws in the design, for example, fiber alignment and understand the interaction between the polymeric structure and the solvents. This work motivated an improved design consisting of using different solvents to resolve the pore structure.

IMPACT AND SIGNIFICANCE

The main goal of this research is to understand and establish processing-structure-property relationships during conversion of renewable sources and by-products into lignin carbon products. With the enormous increase in demand for producing graphite in-house for energy storage applications, the search for graphite

substitutes increased as well. A novel aspect of this research is recycling kraft lignin by-product to produce lignin carbon, that is, identifying a renewable resource as a graphite substitute. The lignin carbon electrode in Li-ion coin cells exhibits promising specific capacities with high Coulombic efficiencies that are comparable with the performance of graphite-based batteries. Characterization experiments support the formation of graphitic domains that mainly depend on the pyrolysis and reduction temperature, the amount of active material, and the anode coating thickness. Moreover, understanding the processing-structure-property relationships for electrochemical applications can serve as support for related research work, such as [85, 86], where molecular dynamics simulations identify differences in the binding mechanism during battery operation between graphite and lignin carbon.

Another significance of these studies is the exploration of processing-structure-property relationships between green and carbon lignin fibers that comes from switchgrass and hardwood, which were organosolv extracted at varying temperature severities. The study validates that switchgrass lignin consists of a polymeric matrix structure that is less smooth and contains smaller pores than hardwood lignin. Statistical analysis identifies a high correlation between tensile strength and phenolic groups of these sources. Using different lignin sources for initial experiments provided insight of how the structure behaves in order to improve the design of the material and prevent defects during processing. Therefore, it is feasible to process lignin sources that can serve in a variety of applications requiring carbon-based materials. Moreover, because the ion binding mechanism of these lignin-based composites is fundamentally different than that seen in graphite, the potential to discover new materials with ion capacities higher than the theoretical capacity of graphite exists.

FUTURE WORK

This research serves as groundwork for designing and performing experiments to further understand processing-structure-property relationships of lignin materials. There still exist several open questions that are of interest and pave a roadmap for potential applications. A full characterization can be conducted for kraft softwood and organosolv switchgrass and hardwood sources before and after each processing stage. It is not

fully understood how the green fiber structure impacts carbonized structure, thus we intend to perform kinetic studies using TGA to understand interactions and thermal stability while processing. The kinetic studies help identify the structural groups that are reacting or changing as well as how fast the reaction occurs. Also, elemental analysis can help us understand the content of C, H, N, and O from the different lignin sources. We also want to look for approaches to prevent reaction between the reduced lignin samples and the nitrogen environment during BET measurements. Additional relationships connecting feedstock structure to carbonized fiber structure include the volume fraction of crystalline domains and crystallite sizes of carbon composites.

Raman and XRD analysis provided different results for particle sizes. To understand the nature of these differences, Raman analysis needs to be performed for the lignin powders and XRD analysis to the carbonized lignin fibers after being grounded. To further understand the differences between switchgrass, yellow poplar, and kraft softwood lignin carbonized structures, Raman analysis needs to be performed for kraft softwood and green lignin, and SANS analysis to lignin carbon. Also, the internal structure of polymeric units can be investigated via molecular dynamics simulations and scatterings from USANS and USAXS. Moreover, we can combine these results with atomistic simulations to interpret lignin carbonaceous structures that are complex due to crystalline and amorphous domains. The computationally-intensive MD simulations can be used to develop a much more computationally efficient but still physics-based approach (a hierarchical decomposition) to interpreting the radial distribution function from scattering experiments.

The high demand for carbon composites in energy storage applications stimulates the search for identifying which lignin source is optimal for battery anodes. Moreover, these studies should include a mix of anodes composed from both lignin fibers and powder. Conveniently, electrochemistry studies should be designed for switchgrass, yellow poplar, and kraft softwood lignin. We suspect battery anodes made of switchgrass lignin will result with optimal electrochemical properties due to its low disordered structure and high lignin purity (due to organosolv fractionation). Nevertheless, kraft softwood lignin seems to be the most viable due to its accessibility for large-scale production and lower processing cost when compared to organosolv

switchgrass and hardwood extraction method. The optimization of the choice of lignin source for manufacture of battery anodes superior to graphite is desired. A method to remove all contaminants that degrade electrochemistry performance needs to be explored. A proposed approach is to decrease all oxygen during heat treatments by varying heating rates and environment. Alternative ball-milling techniques will be explored to reduce contamination.

A cost analysis can be included incorporating the extraction of lignin, the processing of lignin carbon materials, and the targeted application. Correlation of all these analyses will help to fully understand lignin structures paving a path to a low-cost, accessible, and efficient material suitable for large-scale industrial production.

REFERENCES

[1] Heitner C, Dimmel D, Schmidt J. Lignin and lignans: advances in chemistry: CRC press; 2016.
[2] Luo J, Genco J, Cole BJ, Fort RC. Lignin recovered from the near-neutral hemicellulose extraction process as a precursor for carbon fiber. BioResources. 2011;6:4566-93.
[3] Mann DG, Labbé N, Sykes RW, Gracom K, Kline L, Swamidoss IM, et al. Rapid assessment of lignin content and structure in switchgrass (Panicum virgatum L.) grown under different environmental conditions. BioEnergy Research. 2009;2:246-56.
[4] Mendu V, Harman-Ware AE, Crocker M, Jae J, Stork J, Morton S, et al. Identification and thermochemical analysis of high-lignin feedstocks for biofuel and biochemical production. Biotechnology for biofuels. 2011;4:43.
[5] Mussatto SI. Biomass fractionation technologies for a lignocellulosic feedstock based biorefinery: Elsevier; 2016.
[6] Zhang W, Ma Y, Wang C, Li S, Zhang M, Chu F. Preparation and properties of lignin–phenol–formaldehyde resins based on different biorefinery residues of agricultural biomass. Industrial Crops and Products. 2013;43:326-33.
[7] Kubo S, Kadla JF. Kraft lignin/poly (ethylene oxide) blends: effect of lignin structure on miscibility and hydrogen bonding. Journal of Applied Polymer Science. 2005;98:1437-44.
[8] Braun J, Holtman K, Kadla J. Lignin-based carbon fibers: Oxidative thermostabilization of kraft lignin. Carbon. 2005;43:385-94.
[9] Balan V, Bals B, Chundawat SP, Marshall D, Dale BE. Lignocellulosic biomass pretreatment using AFEX. Biofuels: Methods and Protocols. 2009:61-77.
[10] Bozell JJ, Black SK, Myers M, Cahill D, Miller WP, Park S. Solvent fractionation of renewable woody feedstocks: Organosolv generation of biorefinery process streams for the production of biobased chemicals. Biomass and bioenergy. 2011;35:4197-208.
[11] Santos RB, Gomide JL, Hart PW. Kraft Pulping of Reduced Metal Content Eucalyptus Wood: Process Impacts. BioResources. 2015;10:6538-47.
[12] Theliander H. 12 Recovery of Cooking Chemicals: the Treatment and Burning of Black Liquor. Pulping Chemistry and Technology. 2004:297.
[13] Cazacu G, Capraru M, Popa VI. Advances concerning lignin utilization in new materials. Advances in natural polymers: Springer; 2013. p. 255-312.
[14] Johansson A, Aaltonen O, Ylinen P. Organosolv pulping—methods and pulp properties. Biomass. 1987;13:45-65.
[15] McDonough TJ. The chemistry of organosolv delignification. 1992.
[16] Chum H, Johnson D, Black S, Baker J, Grohmann K, Sarkanen K, et al. Organosolv pretreatment for enzymatic hydrolysis of poplars: I. Enzyme hydrolysis of cellulosic residues. Biotechnology and Bioengineering. 1988;31:643-9.
[17] Berlin A, Balakshin MY, Ma R, Maximenko GV, Ortiz D. Organosolv process. Google Patents; 2013.
[18] Ramiah M. Thermogravimetric and differential thermal analysis of cellulose, hemicellulose, and lignin. Journal of Applied Polymer Science. 1970;14:1323-37.
[19] Nordström Y, Norberg I, Sjöholm E, Drougge R. A new softening agent for melt spinning of softwood kraft lignin. Journal of Applied Polymer Science. 2013;129:1274-9.

[20] Rosas JM, Berenguer R, Valero-Romero MJ, Rodríguez-Mirasol J, Cordero T. Preparation of different carbon materials by thermochemical conversion of lignin. Frontiers in Materials. 2014;1:29.
[21] Cullity BD, Stock, S. R. Elements of X-ray diffraction2001.
[22] Anderson IS, McGreevy RL, Bilheux HZ. Neutron imaging and applications. Springer Science+ Business Media. 2009;200:987-0.
[23] Jackson AJ. Introduction to small-angle neutron scattering and neutron reflectometry. NIST Center for Neutron Research, Gaithersburg. 2008:12.
[24] King SM. Small angle neutron scattering. John Wiley & Sons New York; 1999.
[25] Survey G. Mineral Commodity Summaries 2016: Government Printing Office; 2016.
[26] Humphries M. China's mineral industry and US access to strategic and critical minerals: Issues for Congress. Specialist in Energy Policy (March 20, 2015), CRS Report, Congressional Research Service. 2015:7-5700.
[27] Mantell CL. Carbon and Graphite Handbook. 1968.
[28] Van Oss H. US Geological Survey, Mineral Commodity Summaries, January 2013. 2013.
[29] Moss R, Tzimas E, Willis P, Arendorf J, Thompson P, Chapman A, et al. Critical metals in the path towards the decarbonisation of the EU energy sector. Assessing rare metals as supply-chain bottlenecks in low-carbon energy technologies JRC Report EUR. 2013;25994.
[30] Qin H, Kang S, Huang Y, Liu S, Fang Y, Li X, et al. Lignin based synthesis of carbon nanocages assembled from graphitic layers with hierarchical pore structure. Materials Letters. 2015;159:463-5.
[31] Lakes R. Materials with structural hierarchy. Nature. 1993;361:511-5.
[32] Béguin F, Frackowiak E. Carbons for electrochemical energy storage and conversion systems: CRC Press; 2009.
[33] Oyedele A, Mcnutt NW, Rios O, Keffer DJ. Hierarchical Model for the Analysis of Scattering Data of Complex Materials. JOM. 2016:1-6.
[34] Li Z, Lu C, Xia Z, Zhou Y, Luo Z. X-ray diffraction patterns of graphite and turbostratic carbon. Carbon. 2007;45:1686-95.
[35] Kawamoto H. Lignin pyrolysis reactions. Journal of Wood Science. 2017:1-16.
[36] Marsh H, Griffiths J. A high resolution electron microscopy study of graphitization of graphitizable carbon. International symposium on carbon Carbon society of Japan Annual meeting 91982. p. 81-3.
[37] Ferrari AC, Robertson J. Interpretation of Raman spectra of disordered and amorphous carbon. Physical review B. 2000;61:14095.
[38] Aricò AS, Bruce P, Scrosati B, Tarascon J-M, Van Schalkwijk W. Nanostructured materials for advanced energy conversion and storage devices. Nature materials. 2005;4:366-77.
[39] Li J, Daniel C, Wood D. Materials processing for lithium-ion batteries. Journal of Power Sources. 2011;196:2452-60.
[40] Wood DL, Li J, Daniel C. Prospects for reducing the processing cost of lithium ion batteries. Journal of Power Sources. 2015;275:234-42.
[41] Garcia-Negron V, Phillip ND, Li J, Daniel C, Wood D, Keffer DJ, et al. Processing-Structure-Property Relationships for Lignin-based Carbonaceous Materials used in Energy Storage Applications. Energy Technology. 2016.

[42] McNutt NW, Rios O, Feygenson M, Proffen TE, Keffer DJ. Structural analysis of lignin-derived carbon composite anodes. Journal of Applied Crystallography. 2014;47:1577-84.
[43] Faruk O, Sain M. Lignin in Polymer Composites: William Andrew; 2015.
[44] Mainka H, Hilfert L, Busse S, Edelmann F, Haak E, Herrmann AS. Characterization of the major reactions during conversion of lignin to carbon fiber. Journal of Materials Research and Technology. 2015;4:377-91.
[45] Tran H, Vakkilainnen EK. The kraft chemcial recovery process. Tappi Press; 2008.
[46] Reeve D. The kraft recovery cycle, Tappi kraft recovery operations short course. Tappi Press, Atlanta; 2002.
[47] Tenhaeff WE, Rios O, More K, McGuire MA. Highly Robust Lithium Ion Battery Anodes from Lignin: An Abundant, Renewable, and Low-Cost Material. Advanced Functional Materials. 2014;24:86-94.
[48] Ji X, Lee KT, Nazar LF. A highly ordered nanostructured carbon–sulphur cathode for lithium–sulphur batteries. Nature materials. 2009;8:500-6.
[49] Endo M, Kim C, Nishimura K, Fujino T, Miyashita K. Recent development of carbon materials for Li ion batteries. Carbon. 2000;38:183-97.
[50] Vanholme R, Demedts B, Morreel K, Ralph J, Boerjan W. Lignin biosynthesis and structure. Plant physiology. 2010;153:895-905.
[51] Pence HE, Williams A. ChemSpider: an online chemical information resource. Journal of Chemical Education. 2010;87:1123-4.
[52] Cotoruelo L, Marqués M, Díaz F, Rodríguez-Mirasol J, Cordero T, Rodríguez J. Activated carbons from lignin: their application in liquid phase adsorption. Separation Science and Technology. 2007;42:3363-89.
[53] Beis S, Mukkamala S, Hill N, Joseph J, Baker C, Jensen B, et al. Fast pyrolysis of lignins. BioResources. 2010;5:1408-24.
[54] Chatterjee S, Jones EB, Clingenpeel AC, McKenna AM, Rios O, McNutt NW, et al. Conversion of lignin precursors to carbon fibers with nanoscale graphitic domains. ACS Sustainable Chemistry & Engineering. 2014;2:2002-10.
[55] Tarascon J, Armand M. Issues and challenges facing rechargeable lithium batteries. Materials For Sustainable Energy: A Collection of Peer-Reviewed Research and Review Articles from Nature Publishing Group2011. p. 171-9.
[56] Schneider CA, Rasband WS, Eliceiri KW. NIH Image to ImageJ: 25 years of image analysis. Nat methods. 2012;9:671-5.
[57] Watkins D, Nuruddin M, Hosur M, Tcherbi-Narteh A, Jeelani S. Extraction and characterization of lignin from different biomass resources. Journal of Materials Research and Technology. 2015;4:26-32.
[58] Singh K, Risse M, Das K, Worley J. Determination of composition of cellulose and lignin mixtures using thermogravimetric analysis. Journal of Energy Resources Technology. 2009;131:022201.
[59] Bard AJ, Faulkner LR, Leddy J, Zoski CG. Electrochemical methods: fundamentals and applications: Wiley New York; 1980.
[60] Leitner SP, Gratzl G, Paulik C, Weber HK. Carbon Materials from Lignin and Sodium Lignosulfonate via Diisocyanate Cross-Linking and Subsequent Carbonization. C. 2015;1:43-57.

[61] Goudarzi A, Lin L-T, Ko FK. X-Ray Diffraction Analysis of Kraft Lignins and Lignin-Derived Carbon Nanofibers. Journal of Nanotechnology in Engineering and Medicine. 2014;5:021006.
[62] Degen T, Sadki M, Bron E, König U, Nénert G. The highscore suite. Powder Diffraction. 2014;29:S13-S8.
[63] McNutt NW. Lignin-based Li-Ion Anode Materials Synthesized from Low-Cost Renewable Resources. 2016.
[64] An SJ, Li J, Daniel C, Mohanty D, Nagpure S, Wood DL. The state of understanding of the lithium-ion-battery graphite solid electrolyte interphase (SEI) and its relationship to formation cycling. Carbon. 2016;105:52-76.
[65] Goriparti S, Miele E, De Angelis F, Di Fabrizio E, Zaccaria RP, Capiglia C. Review on recent progress of nanostructured anode materials for Li-ion batteries. Journal of Power Sources. 2014;257:421-43.
[66] Perlack RD, Wright LL, Turhollow AF, Graham RL, Stokes BJ, Erbach DC. Biomass as feedstock for a bioenergy and bioproducts industry: the technical feasibility of a billion-ton annual supply. DTIC Document; 2005.
[67] Hosseinaei O, Harper DP, Bozell JJ, Rials TG. Role of Physicochemical Structure of Organosolv Hardwood and Herbaceous Lignins on Carbon Fiber Performance. ACS Sustainable Chemistry & Engineering. 2016.
[68] Imel AE, Naskar AK, Dadmun MD. Understanding the Impact of Poly (ethylene oxide) on the Assembly of Lignin in Solution toward Improved Carbon Fiber Production. ACS applied materials & interfaces. 2016;8:3200-7.
[69] Kadla JF, Kubo S, Gilbert RD, Venditti RA. Lignin-based carbon fibers. Chemical Modification, Properties, and Usage of Lignin: Springer; 2002. p. 121-37.
[70] Jin W, Singh K, Zondlo J. Pyrolysis kinetics of physical components of wood and wood-polymers using isoconversion method. Agriculture. 2013;3:12-32.
[71] Sannigrahi P, Ragauskas AJ, Tuskan GA. Poplar as a feedstock for biofuels: a review of compositional characteristics. Biofuels, Bioproducts and Biorefining. 2010;4:209-26.
[72] Petridis L, Pingali SV, Urban V, Heller WT, O'Neill HM, Foston M, et al. Self-similar multiscale structure of lignin revealed by neutron scattering and molecular dynamics simulation. Physical Review E. 2011;83:061911.
[73] Cheng G, Zhang X, Simmons B, Singh S. Theory, practice and prospects of X-ray and neutron scattering for lignocellulosic biomass characterization: towards understanding biomass pretreatment. Energy & Environmental Science. 2015;8:436-55.
[74] Cheng G, Kent MS, He L, Varanasi P, Dibble D, Arora R, et al. Effect of ionic liquid treatment on the structures of lignins in solutions: molecular subunits released from lignin. Langmuir. 2012;28:11850-7.
[75] Calo J, Hall P, Antxustegi M. Carbon porosity characterization via small angle neutron scattering. Colloids and Surfaces A: Physicochemical and Engineering Aspects. 2001;187:219-32.
[76] Dresselhaus M, Jorio A, Souza Filho A, Saito R. Defect characterization in graphene and carbon nanotubes using Raman spectroscopy. Philosophical Transactions of the Royal Society of London A: Mathematical, Physical and Engineering Sciences. 2010;368:5355-77.

[77] Li HWYWT, Xu SWL. Gradient distribution of radial structure of PAN-based carbon fiber treated by high temperature.
[78] Ferrari AC, Basko DM. Raman spectroscopy as a versatile tool for studying the properties of graphene. Nature nanotechnology. 2013;8:235-46.
[79] Navarro-Suárez AM, Carretero-González J, Roddatis V, Goikolea E, Ségalini J, Redondo E, et al. Nanoporous carbons from natural lignin: study of structural–textural properties and application to organic-based supercapacitors. RSC Advances. 2014;4:48336-43.
[80] Boota M, Paranthaman MP, Naskar AK, Li Y, Akato K, Gogotsi Y. Waste Tire Derived Carbon–Polymer Composite Paper as Pseudocapacitive Electrode with Long Cycle Life. ChemSusChem. 2015;8:3576-81.
[81] Sammons RJ, Harper DP, Labbé N, Bozell JJ, Elder T, Rials TG. Characterization of organosolv lignins using thermal and FT-IR spectroscopic analysis. BioResources. 2013;8:2752-67.
[82] Tsaneva V, Kwapinski W, Teng X, Glowacki B. Assessment of the structural evolution of carbons from microwave plasma natural gas reforming and biomass pyrolysis using Raman spectroscopy. Carbon. 2014;80:617-28.
[83] Tuinstra F, Koenig JL. Raman spectrum of graphite. The Journal of Chemical Physics. 1970;53:1126-30.
[84] Wang H, Wang Y, Li T, Wu S, Xu L. Gradient distribution of radial structure of PAN-based carbon fiber treated by high temperature. Progress in Natural Science: Materials International. 2014;24:31-4.
[85] McNutt NW, McDonnell M, Rios O, Keffer DJ. Li-Ion Localization and Energetics as a Function of Anode Structure. ACS Applied Materials & Interfaces. 2017;9:6988-7002.
[86] McNutt NW, Rios O, Maroulas V, Keffer DJ. Interfacial Li-ion localization in hierarchical carbon anodes. Carbon. 2017;111:828-34.

VITA

Valerie García-Negrón was born in Ponce, Puerto Rico on January 1, 1988. She obtained her Bachelor of Science in Chemical Engineering from the Polytechnic University of Puerto Rico in April 2012. Previous to obtaining the bachelor degree, in summer 2010 she worked under the mentoring of Dr. Edgar Lara-Curzio from Material Sciences and Technology Division at Oak Ridge National Laboratory. She worked in different projects mainly for fuel cells research using ceramic sealing application and studying microstructural and thermal characterization of these materials. She also worked with processing magnets materials where Dr. Orlando Rios hosted her. In conjunction to Dr. Rios and Dr. Lara-Curzio she started working with Dr. David Harper in September 2014 at Center for Renewable Carbon at University of Tennessee-Knoxville. Then, in spring 2015 she planned to study at the University of Tennessee to continue her professional career in Materials Science and Engineering Department. Under MSE department she was mentored by Dr. David Keffer were he led her studies. She planned to obtain her Master of Science degree in Material Sciences and Engineering in May 2017. In between research and class environment she was part of two invention disclosures. Her current interests are mainly research environment and continue her PhD in Materials Science and Engineering. She wants to travel the world, learn a third language, learn to dance salsa, and spend quality time with her family in Puerto Rico.